UNDERSTANDING ELECTRON TRANSFER PROCESSES WITH MULTISCALE QUANTUM CHEMISTRY METHODS

BY PABLO RAMOS

A dissertation submitted to the

Graduate School-Newark

Rutgers, the State University of New Jersey

In partial fulfillment of the requirements

for the degree of

Doctor of Philosophy

Graduate Program of Chemistry

written under the direction of

Professor Michele Pavanello

and approved by

_____

_____

_____

_____

Newark, New Jersey

May, 2018

Abstract

The research described in this dissertation consists of two projects. First, the application and improvement of a subsystem DFT method to describe charge transfer reactions in biosystems and molecular materials. Second, the development and validation of a constrained subsystem DFT method to model charge and excitation energy transfer processes in molecules and condensed phases.

After introducing the theory of charge transfer reactions in condensed phases (chapter 1), the candidate outlines original and well-established avenues to obtain the electronic couplings (the key parameter to understand the dynamics of these processes). The first project is presented in chapter 3, in which a benchmark study against high-level methods is presented followed by the analysis of the environmental effects on the hole transfer in DNA oligomers. In chapter 4 the advantages of the candidate's method are pointed out, especially its ability to combine Constrained DFT and subsystem DFT formalisms. Such a flexible method enables the study of the effects of the phosphate group on hole transfer couplings in DNA for the first time in the literature. Additional applications of this method are given in chapter 5, where the quality of the calculated excited states is examined. Finally, in the last chapter two applications are presented: modeling of (1) the hole transfer in Fe-TPP dyads; and (2) charge transfer in the peptidylglycine-α-hydroxylating monooxygenase enzyme.

Every project is published or in the process to be published by the candidate

in co-authorship with the candidate's scientific advisor and other collaborators in peer-reviewed journals.

Dedication

A mi amada $\mathcal{L}$una, verte reir es mi hazaña mas justa, mi cimiento inexpugnable, mi amor enternecido.

Acknowledgements

I would like to express my gratitude to Prof. Pavanello for his support along my PhD study. Thank you Michele for the good moments inside and outside the lab. It was a real pleasure to be in your lab and tackle the nice challenges that help us to be better professionals. I appreciate the time you took to guide me overcome several academic and personal situations. I admire your energy and resourceful knowledge in Theoretical Chemistry, it is really an inspiration and it will have a significant effect on my professional career. It has been an honor be part of this group and be your student.

I want to thank my thesis committee members, Prof. Lockard, Prof. Piotrowiak and Dr. Wu for their time, interest and insightful discussions and comments to this work.

I am indebted to my family, my courageous wife $\mathcal{D}$aniela and my little beautiful $\mathcal{L}$una. Which with their unfailing love, patience and smiles, They have been my pillar and the indefatigable fuel in this way. I should mention the support of my relatives, my father Raul, my mother Emilia and my sister Laura.

I would like to thank Saikat, Zheng 'Vivid', Shugo, Marc, Aisha and King for their friendship here and in distant lands away from home.

I want to thank my colleagues, Rupali, Alessandro, Sudheer, Wenhui, Alina, Johanes, Ruslan, Alisa and Debalina with whom I had great time working, enjoying life outside the lab, sharing peanuts and discussing. I am glad to have spent some time

with you. Thanks for your friendship and camaraderie.

I would also like to thank the Chemistry department, and Judy Slocum in particular, for all help throughout these years.

Contents

List of Figures

List of Tables

Chapter 1

Introduction

Charge transfer (CT) plays an important role in processes that occur in biology (DNA oxidative damage, protein communication) as well as in materials science (processes such as, conduction in molecular semiconductors, recombination at interfaces, etc). In order to achieve accurate yet realistic models of these processes, the scientific community often needs to include several layers of complexity. In most cases this leads to contemplate model systems containing hundreds-to-thousands of atoms and an even larger number of electrons.

Such large system sizes preclude the use of high-level wavefunction-based quantum-chemical methods. These methods are impractical because complexity of their algorithms exceeds the computational resources available today. Researchers have tackled this problem head-on and have invested efforts into developing fast-yet-accurate methods for modeling CT reactions. In this regard, methods based on Density-Functional Theory (DFT, hereafter) especially popular because they provide a satisfactory range of accuracy and low computational cost.

Eventhough DFT methods reduce the computational effort substantially, chemistry experiments rarely treats isolated molecules. Also, environmental effects are sometimes crucial to understand the physical implications of chemical process. Thus,

typical DFT methods are still computationally too expensive for modeling realistically sized systems. Subsytem DFT aims at solving this issue. It partitions the electron density of a system in many smaller subsystems densities. Among the various flavors of subsystem DFT, the Frozen Density Embedding (FDE) method provides a simple and easy to implement prescription. In short, the subsystems composing the supramolecular system interact through an embedding potential, where all the interaction (nonadditive) terms are considered. In this thesis, we tackle the computational cost employing FDE. However, there is still a problem related to modeling CT processes. How can this be achieved with susbsystem DFT?

Before entering in the details of the actual electronic structure methods, let us introduce the framework at the foundation of this work: Marcus theory of electron transfer. Marcus theory[65] is perhaps the most applicable theory for modeling a CT process. It was originally derived under three main approximations. First, a CT event is thought of in terms of a two-dimensional basis set of diabatic states (donor state and acceptor state). The interaction matrix element (i.e., the off-diagonal element of the Hamiltonian matrix in this basis) is the central quantity for determining the probability of a transition between the donor state and the acceptor state. We name this interaction electronic coupling, V_{DA}. Second, it relies on the Condon approximation, in which the electronic coupling is considered to be independent of the nuclear motion when the CT occurs. Third, in its original formulation, reactants and products are modeled as being enclosed by spheres on which the polarization of the solvent is represented as a dielectric continuum. The rate constant of CT in Marcus theory is given by [84],

$$k_{CT} = \frac{2\pi}{\hbar} |V_{DA}|^2 \frac{e^{-\frac{(\Delta G + \lambda)^2}{4\lambda K_B T}}}{\sqrt{4\pi\lambda K_B T}}, \tag{1.1}$$

where λ is the reorganization energy, and V_{DA} is the electronic coupling. States that most resemble the initial and final states of electron transfer are often referred

to as "diabatic states" and their corresponding wavefunctions "diabats". Although it is known that diabatic states have a formal definition [60], it was shown [90] that charge-localized states satisfy the requirements for diabatic states for condensed phase electron transfer reactions.

Three fast, reliable and all-electron methods to tackle charge transfer processes in realistic size systems are herein proposed. The FDE-ET (ET stands for Electron Transfer) is an extension of the capabilities given by the FDE method tailored for modeling physically accurate diabatic states needed (charge localized states). Such diabatic states can be generated by imposing a charge (either positive or negative) onto the donor subsystem while the acceptor remains neutral and in the same way but this time the charge will be in the acceptor. However, FDE can be only applied to systems that posses noncovalently bond subsystems.

In order to cure this limitation of the FDE method, the Constrained DFT (CDFT) method is employed when diabatic states need to be considered on with charge localization within a molecule. CDFT ensures the localization of an electronic charge on a specific place on the system without needing to cut bonds. Charge localization in CDFT is achieved by applying an additional potential that lures the electron density to satisfy a given constraint. FDE and CDFT methods can be coupled into a single versatile method: the Constrained Subsystem DFT (CSDFT) approach. CS-DFT aims to eliminate the limitations existed under the FDE scheme. Due to its philosophy, FDE applicability is restricted to those transfers that occur from two (or more) non-covalently bonded molecules. Therefore, CSDFT ensures the construction of a diabatic state and also allows the inclusion of the environmental effects on the energetics of these diabatic states using the FDE strategy.

Complementary, the implementation of a novel option to compute excited states is explored. The eXcited Constrained DFT or XCDFT method, is a time–independent method that resolves the space of virtuals by projection. Thus, the Fock operator is

augmented by a nonlocal constraining potential that exerts a force, pulling electrons into the virtual space. As before, XCDFT can be utilized to obtain reliable excitations in complex systems maintaining low computational penalty.

In this dissertation, the candidate first explains the theory behind charge transfer reactions, in particular the evaluation of the electronic coupling quantum mechanically with the FDE-ET method. Afterwards, two applications of FDE-ET are presented. In the second part of the dissertation, the candidate introduces CSDFT and XCDFT algorithms. Both methodologies are implemented by the candidate in the Amsterdan Density Functional (ADF) suite of programs. In each case, pros and cons of the method are analyzed. At the end of each chapter a significant application study is provided to showcase the qualities of the theory and software development.

Chapter 2

Modeling Charge Transfer Reactions With Subsystem DFT: The FDE-ET Method

This Chapter is adapted from the following peer–reviewed journals

- Pablo Ramos and Michele Pavanello. Quantifying Environmental Effects on the Decay of Hole Transfer Couplings in Biosystems. J. Chem. Theory Comput.,10:2546–2556, 2014.

- Pablo Ramos and Michele Pavanello. Performance of Frozen Density Embedding for Modeling Hole Transfer Reactions. J. Phys. Chem. B, 119:7541–7557, 2015.

2.1 Background on FDE

In the FDE formalism the total electron density is expressed as the sum of subsystem electron densities[123, 104, 19]. Namely,

$$\rho_{tot}(\mathbf{r}) = \sum_{I=1}^{N_s} \rho_I(\mathbf{r}). \tag{2.1}$$

Where N_s is the number of subsystems.

For each subsystem the electron density is obtained by solving a Kohn–Sham (KS) like equation. The KS–Hamiltonian is augmented by an embedding potential that accounts for the interactions between subsystems. However, the electron density of those subsystems is kept frozen in this step, the KS equation reads as

$$\left[\frac{-\nabla^2}{2} + v_{KS}^I(\mathbf{r}) + v_{emb}^I(\mathbf{r}) \right] \phi_{(i)I}(\mathbf{r}) = \epsilon_{(i)I}(\mathbf{r})\phi_{(i)I}(\mathbf{r}). \tag{2.2}$$

Where $\phi_{(i)I}(\mathbf{r})$ are the molecular orbitals of subsystem I, and $v_{emb}^I(\mathbf{r})$ is the embedding potential acting on the same subsystem and is defined as follows:

$$v_{emb}^I(\mathbf{r}) = \sum_{J \neq I}^{N_s} \left[\int \frac{\rho_J(\mathbf{r}')}{|\mathbf{r} - \mathbf{r}'|} d\mathbf{r}' - \sum_{\alpha \in J} \frac{Z_\alpha}{|\mathbf{r} - \mathbf{R}_\alpha|} \right] +$$
$$+ \frac{\delta T_s[\rho]}{\delta \rho(\mathbf{r})} - \frac{\delta T_s[\rho_I]}{\delta \rho_I(\mathbf{r})} + \frac{\delta E_{xc}[\rho]}{\delta \rho(\mathbf{r})} - \frac{\delta E_{xc}[\rho_I]}{\delta \rho_I(\mathbf{r})}. \tag{2.3}$$

The terms T_s, E_{xc} and Z_α are kinetic and exchange–correlation energy functionals, and the nuclear charge, respectively. Due to the nature of the KS method, $T_s[\rho]$ is obtained from the molecular orbitals of the entire system. However, these orbitals are not calculated in FDE and therefore approximate kinetic energy functionals are employed instead. In which the non-additive kinetic energy (NAKE) term is represented with a semilocal functional. The use of these approximate functional are the biggest difference between an FDE and a full KS-DFT calculation of the supersystem[39, 122, 62].

In the case of large overlap between subsystem electron densities, FDE in conjunction with GGA NAKE functionals becomes unreliable when compared to regular KS-DFT [33, 51]. To achieve selfconsistency, the subsystem densities are determined in an iterative way called freeze-and-thaw [124, 47].

2.2 How does FDE generate diabats?

In practical terms, an FDE calculation is performed on at least two interacting subsystems (donor and acceptor fragments) whose electron densities are determined selfconsistency via the freeze-and-thaw procedure. Given by the freeze-and-thaw procedure two simulations are set up: in one a hole is placed on the donor fragment (i.e., the KS-like equations are solved in such a way the density of the donor fragment integrates to a number of electrons defecting by one compared to the neutral fragment), in the second calculation the acceptor is now positively charged. We can revert the situation by increasing the number of electrons by one – an excess electron is generated on the subsystem. The result of the freeze-and-thaw procedure is that the charge, either a hole or an electron, is completely localized onto the fragment (donor or acceptor).

An FDE calculation yields charge localize states [92] due to the following reasons: first, the subsystem orbitals are not imposed to be orthogonal to orbitals of the other subsystems. This is important as it implies that not imposing orthogonality removes a bias towards delocalization, as noted by Dulak and Wesolowski [23]. However, this reason alone is not enough. A second reason is that FDE calculations are carried out in the monomer basis set [i.e., using the FDE(m) method [46]]. With no basis functions on the surrounding frozen subsystems, a charge transfer between the subsystems becomes an unlikely event and the SCF is biased to converge to a charge localized solution. The third reason invokes the fact that FDE calculations are always initiated with a subsystem localized guess density. The initial conditions also have a bias effect

υ^I_{emb}

Atom in a Frozen Subsystem
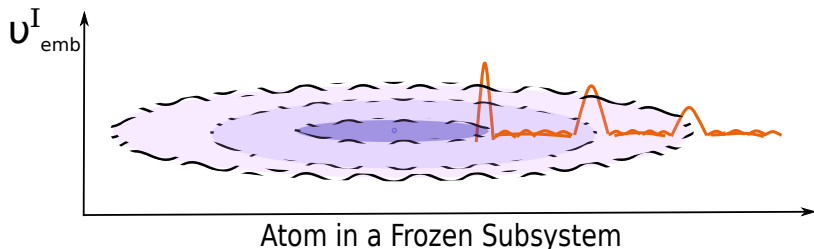
Figure 2.1: Depiction of the shape of the embedding potential (in red) in the region of the atomic shells of surrounding subsystems. Reproduced with permission from reference 98

on the final SCF solution – a localized initial guess density will likely yield an SCF solution that is subsystem localized as well. Finally, the shape of the embedding potential in the region of the surrounding fragments. Electrons remain localized also because there are repulsive walls in the vicinity of the atomic shells of atoms belonging to the surrounding subsystems. The approximate kinetic energy functionals are unable to cancel out the attractive potential due to the nuclear charge in the vicinity of the nucleus. However, the shape of most semilocal kinetic energy potentials is such that in going towards the nucleus they start out too low compared to the exact potentials, then cross the exact potential and become larger in the region of an atomic shell. For a simplify picture of this behavior see Figure 2.1

2.3 Coupling calculations with FDE: the FDE-ET method

The electronic coupling between non-orthogonal wavefunctions (approximated at DFT level yet exact under Hartree–Fock theory) can be expressed as [92, 113, 25]:

$$H_{DA} = \langle \psi_D | \hat{H} | \psi_A \rangle = S_{DA} E \left[\rho^{(DA)}(\mathbf{r}) \right] . \tag{2.4}$$

where $\hat{H}$ is the molecular electronic Hamiltonian, ψ_D and ψ_A are the two diabatic states (D for donor, A for acceptor) and $\rho^{(DA)}(\mathbf{r})$ is the transition density defined as follows:

$$\rho^{(DA)}(\mathbf{r}) = \langle \psi_D | \sum_{k=1}^{\#ofelectrons} \delta(\mathbf{r}_k - \mathbf{r}) | \psi_A \rangle \tag{2.5}$$

If the wavefunctions are expressed in terms of single Slater determinants, the overlap element appearing in Eq. (2.5) is determined by the following determinant:

$$S_{DA} = \det \left[\mathbf{S}^{(DA)} \right], \tag{2.6}$$

where $\mathbf{S}_{kl}^{DA} = \langle \phi_k^{(D)} | \phi_l^{(A)} \rangle$ is the transition overlap matrix in terms of the occupied orbitals $(\phi_{k/l}^{(D/A)})$[70, 113]. In this manner, the transition density is neatly written in the basis of all occupied orbitals that constitute both the diabatic states ψ_D and ψ_A. Namely,

$$\rho^{(DA)}(\mathbf{r}) = \sum_{kl}^{occ} \phi_k^{(D)}(\mathbf{r}) \left(\mathbf{S}^{(DA)} \right)_{kl}^{-1} \phi_l^{(A)}(\mathbf{r}). \tag{2.7}$$

Transferring the above equations to model charge transfer (CT) reactions, we start by construction of two diabatic states: a state where the charge is on the donor (D) also called initial state, and a state where the charge is on the acceptor (A). However, by construction one should not expect that the charge localized states are necessarily eigenstates of the molecular Hamiltonian of the total system, due to their non-orthogonal nature. Thus, we expect the Hamiltonian and overlap matrix to be non-diagonal. The Hamiltonian and overlap matrices are then written in terms of this non-orthogonal basis. Namely,

$$\mathbf{H} = \begin{pmatrix} H_{DD} & H_{DA} \\ H_{AD} & H_{AA} \end{pmatrix}, \quad \mathbf{S} = \begin{pmatrix} 1 & S_{DA} \\ S_{AD} & 1 \end{pmatrix}. \tag{2.8}$$

where the off–diagonal elements are given by equation 2.4. However, the Hamiltonian coupling is not H_{DA}, but it is generally reported as the coupling between the

Löwdin orthogonalized ψ_D and ψ_A. For only two states this takes the form,

$$V_{DA} = \frac{1}{1 - S_{DA}^2} \left(H_{DA} - S_{DA} \frac{H_{DD} + H_{AA}}{2} \right), \qquad (2.9)$$
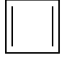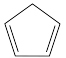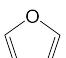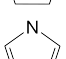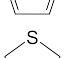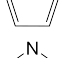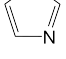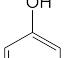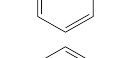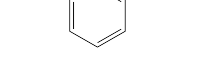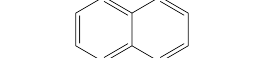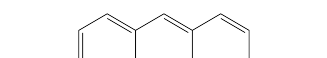
2.4   Distance dependence of the electronic coupling

In this section, we discuss calculations of the coupling matrix element (V_{DA}) of hole transfer from a donor to an acceptor molecule through the vacuum. This means that the initial state of hole transfer is the donor molecule (D), and the final state the acceptor molecule (A), and no intermediate bridge states are considered. Overall, our couplings show a good agreement with previous computations (e.g. we reproduced the decay factors, β, π-stacked dimers separated by vacuum).

When the HAB11 test set featuring high accuracy couplings became available [1], we compare systematically the FDE-ET couplings with the benchmark values [98]. Benchmark calculations were ran on a set of 15 of π-stacked dimers (see Table 2.1).

This study was rigorous, and tested the effect of the basis set size, nonadditive kinetic energy functionals (NAKE) and exchange-correlation functionals (XC) on the value of the computed couplings. The most important finding that resulted from the benchmark work resided in the fact that GGA functionals coupled with a medium sized basis set and the PW91k NAKE functional allow the FDE-ET method to yield reliable electronic couplings as tested against high-level correlated wavefunction (MRCI+Q, NEVPT2 and SCS-CC2) methods applied to the array of dimers. The PBE and PW91 functionals are found to be a good choice in each case considered with a MAX error lower than 50 meV and an overall MRUE of a little over 7% in both cases[98].

Statistically, we found that hole transfer couplings are relatively insensitive to the choice of NAKE functionals, while our analysis of the basis set dependence shows that

Dimer	Symbol[a]	Structure	Reference method[b]
Ethylene	(EE)	$H_2C\!=\!CH_2$	MRCI+Q
Acetylene	(AC)	$HC\!\equiv\!CH$	MRCI+Q
Cyclopropene	(CP)		MRCI+Q
Cyclbutadiene	(CB)		MRCI+Q
Cyclopentadiene	(CD)		MRCI+Q
Furane	(FF)		MRCI+Q
Pyrrole	(PY)		MRCI+Q
Thiophene	(TH)		NEVPT2
Imidazole	(IM)		NEVPT2
Phenol	(PH)		NEVPT2
Benzene	(BB)		NEVPT2
Naphthalene	(NN)		SCS-CC2
Anthracene	(AA)		SCS-CC2
Tetracene	(TT)		SCS-CC2
Pentacene	(PP)		SCS-CC2

a Abbreviations used in this work.
b Ref.1

Table 2.1: Dimers of the HAB11 test set. Reproduced with permission from reference 98

QZ4P basis set is the most problematic, as it often biases the FDE convergence to nonphysical states at short intersubsystem separations – a problem already well documented in the FDE literature[31, 30]. Finally, Table 3.1 compares the performance of FDE-ET for different levels of theory. The results for GGAs are in good agreement with the benchmark values, and in some cases they showed to be superior to hybrid and meta-GGA functionals, particularly PBE and PW91. B3LYP also stands out as another valuable choice.

Generally, all functionals perform well in the FDE-ET coupling calculations making FDE-ET a method that is relatively insensitive to the XC and NAKE functional choice.

Set	MUE(MeV)	MRUE(%)	MAX(meV)
PBE/PW91k/TZP	15.3	7.1	49.6
PW91/PW91k/TZP	15.2	7.1	49.1
B3LYP/PW91k/TZP	18.1	7.9	58.5
M06-2X/PW91k/TZP	18.0	8.2	54.9

Table 2.2: Mean statistical values for the best XC-functional choices. PW91k is the NAKE along this work. Reproduced with permission from reference 98

2.5   Hole transfer in DNA oligomers

The electronic coupling for hole transfer in a completely dry B-DNA structure of $G(T)_N G$ and $G(A)_N G$ was calculated. The structures considered in this analysis lack water molecules, metal counterions and phosphate linker groups. The latter is consequence of the applicability of FDE, which is restricted to non-covalently bound fragments. Consequently, appropriate modifications to the B-DNA structure had to be made: we first removed the phosphate groups (PO_4) and capped the dangling bonds with hydrogen atoms at 1.09 Å from the bonding atom. The modified structure $G(T)_N G$ is ilustrated in Figure 2.2. Due to the FDE scheme we were able to considered

308 atoms and 1322 electrons, where the counterstrand as well as the ribose groups were taken into account. In this study, the role of the environment on the hole transfer in DNA is elucidated and analyzed using a full–electron methodology.

Due to the $\begin{pmatrix} T \\ A \end{pmatrix}_N$ bridge separating donor and acceptor assists the hole transfer by lowering the effective tunneling barrier. We computed this effect by considering the full Hamiltonian and overlap matrices of the hole pseudoparticle defined in Eqs. (2.4–2.6). Namely,

$$\mathbf{H} = \begin{pmatrix} E_D & ... & H_{DA} \\ \vdots & \mathbf{H}_B & \vdots \\ H_{AD} & ... & E_A \end{pmatrix}, \ \mathbf{S} = \begin{pmatrix} 1 & ... & S_{DA} \\ \vdots & \mathbf{S}_B & \vdots \\ S_{AD} & ... & 1 \end{pmatrix}. \tag{2.10}$$

In the matrices above, a clear distinction between matrix elements between states where the hole is localized on the bridge molecules or on the donor and acceptor molecule has been labeled. If we considered that during the hole tunneling the bridge states are virtually occupied by the hole, an effective coupling can be obtained by reducing the generalized eigenvalue problem constructed with the above Hamiltonian and overlap matrices to a 2×2 effective eigenvalue problem [71, 110]. A Löwdin orthogonalization of the basis set yields a transformed Hamiltonian matrix, $\tilde{\mathbf{V}}$, from which the following bridge-mediated effective hole coupling is derived [26, 83, 61, 57, 96]:

$$V_{DA}(E) = \tilde{V}_{DA} + \underbrace{\tilde{\mathbf{V}}_{DB}^T \mathbf{G}_B(E) \tilde{\mathbf{V}}_{BA}}_{V_{\text{bridge}}}, \tag{2.11}$$

where the superscript T stands for transpose, $\mathbf{G}_B(E)$ is the Green's operator, defined as

$$\mathbf{G}_B(E) = -(\tilde{\mathbf{V}}_B - E \, \tilde{\mathbf{I}}_B)^{-1}, \tag{2.12}$$

and $\tilde{\mathbf{V}}_{DB/BA}$ is the row vector of the transformed Hamiltonian collecting the couplings

between the donor/acceptor with the bridge states. Generally, E appearing above is the energy at which the tunneling event occurs (i.e. at the crossing seam of the Marcus parabolas). As we only considered static geometries of the DNA oligomers, the Hamiltonian eigenvalues corresponding to the donor-acceptor energies do not coincide. With that, the tunneling energy, E, is not well defined [66]. A natural choice of E is to place it between E_A and E_B, with a common choice being $\frac{E_D+E_A}{2}$. For example, this choice is invoked by several works in the literature [43, 83, 66, 118]. Others[116], have favored the choice $E = E_D$, which is non-symmetric (i.e. forward CT become not equivalent to backward CT), however, it is still a valid choice. It was Marcus [66] who first showed the mild dependence of the coupling with respect to the choice of tunneling energy within E_D and E_A. Thus, we adopt $E = \frac{E_D+E_A}{2}$ in all calculations.

Turning to the results of this study, it was noticed that an uneven stabilization of the bridge states compared to donor/acceptor states occurs in both type of oligomers, this effect is more pronounced in the $G(T)_N G$ system than in the $G(A)_N G$ system. By inspection of the overall electrostatics of the interaction between G:C and T:A [77], we notice that T has a strong permanent dipole pointing towards A, similarly to C:G. Instead, A has a much weaker dipole compared to C or T and thus upon contact of the GTG strand with the CAC strand the cytosines will stabilize much more the holes on Gs than the adenines can stabilize the holes on Ts, hence the tunneling wall increases from single strand to double strand.

Regarding the couplings, when the magnitude of the through space and through bridge couplings are inspected, our calculations show that the effects of the ribose groups and the nucleobases in the counterstrand are opposite and different in magnitude depending on the oligomer size (see table 2.3). We conclude, however, that the effect of the counterstrand on the computed superexchange couplings completely overpowers any effect due to the presence of the ribose groups.

	$\tilde{V}_{DA}$ (meV)	V_{bridge} (meV)	E_{DB} (eV)	E_{BA} (eV)
SINGLE STRAND NO RIBOSE				
GG	78.13			
GTG	0.76	12.46	0.71	0.50
G(T)$_2$G	0.01	1.13	0.79	0.66
G(T)$_3$G	–	0.09	0.79	0.77
DOUBLE STRAND NO RIBOSE				
GG	92.6			
GTG	0.65	7.66	0.93	0.96
G(T)$_2$G	0.01	0.47	1.11	0.94
G(T)$_3$G	–	0.02	0.99	1.16
SINGLE STRAND WITH RIBOSE				
GG	71.38			
GTG	0.18	25.01	0.43	0.37
G(T)$_2$G	0.02	1.70	0.58	0.37
G(T)$_3$G	–	0.21	0.41	0.41
DOUBLE STRAND WITH RIBOSE				
GG	91.07			
GTG	0.02	7.35	0.62	0.87
G(T)$_2$G	0.02	0.61	0.93	0.60
G(T)$_3$G	–	0.02	0.50	0.82

Table 2.3: Through-space and through-bridge electronic coplings and tunneling energy gaps for single and double strand G(T)$_N$G B-DNA, including the effects of the backbone (sugars). A – is shown for values below 0.01meV. Reproduced with permission from reference 97.
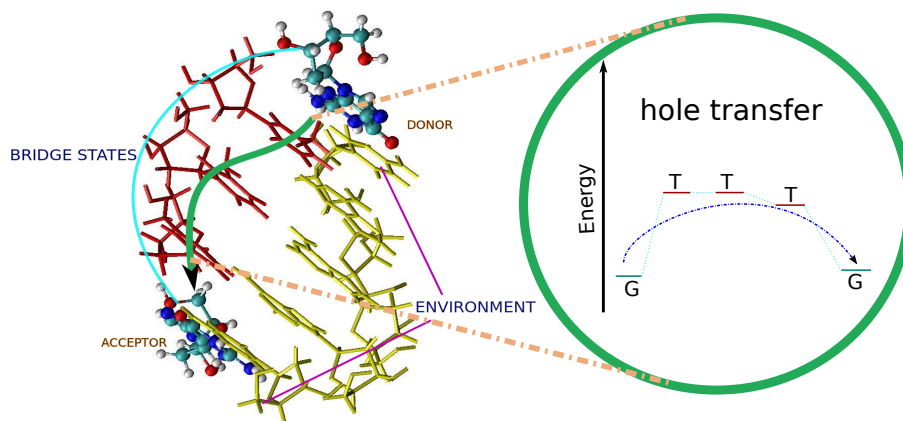
Figure 2.2: The dephosphorilated $G(T)_N G$ B-DNA oligomer employed in the hole transfer coupling calculations. As the figure depicts, the hole tunnels from the bottom guanine (in balls and sticks) to the top guanine. The tunneling wall is provided by a series of three thymines (red branch, labeled as "bridge"). The counterstrand, $C(A)_N C$, acts as a solvating environment (in yellow, labeled as "spectators") and no hole is allowed to localize on it. Reproduced with permission from reference 97.

When the through space and through bridge couplings are inspected, our calculations show that the effects of the ribose groups and the nucleobases in the counterstrand are opposite and different in magnitude depending on the oligomer size. We conclude, however, that the effect of the counterstrand completely overpowers any effect due to the presence of the ribose groups. Nevertheless, the major limitation of our calculations rests in the absence of nuclear dynamics. As dynamics plays a major role in modulating the couplings and energies in biological hole transfer, we commit to investigate such dynamical effects in a follow up work.

Chapter 3

Linking Donor and Acceptor States: The Constrained Subsystem DFT Method

This Chapter is adapted from the following peer–reviewed journal

- Pablo Ramos and Michele Pavanello. Constrained Subsystem Density-Functional Theory. Phys. Chem. Chem. Phys., 18:21172, 2016.

3.1 Introduction

Constrained DFT (CDFT) [20, 114, 49] is a formulation of KS-DFT that, in many instances [69], allows the description of charge transfer phenomena in a quantitative way even if the LDA or GGA approximations are employed in the density functional. CDFT has been widely used not only in charge transfer reactions (with molecular basis set[49] or plane waves basis set[85]) but also in ordinary chemical reactions[127], magnetic properties and excited states[25, 21].

Similarly to KS-DFT, CDFT scales with the cube of system size. Although poly-

nomial, such a scaling becomes computationally intractable when tackling realistically-sized molecular systems and materials. Tremendous effort has been made towards the development of new DFT based methods and their implementations (see for example, Refs. [8]) that can afford simulating thousands of atoms. Along these efforts, our group has worked to advance density embedding methods, such as frozen density embedding (FDE) [123], extending both its theoretical and computational applicability [55] in an effort to produce simulations of molecules and materials that scale almost linearly with system size [37]. FDE has been developed for some time now, and it has been successfully employed to model a number of physical processes, such as excited states[125, 81, 15, 89, 82], magnetic properties [48, 10, 50], and charge transfer processes[97, 92, 111, 98].

In this work, we introduce a new method that combines the strengths of FDE with the ones of CDFT. We call this method constrained subsystem DFT (CSDFT, hereafter). To achieve it, at least two new constraints need to be included in the KS-DFT Lagrangian (see the Theory section). The aims of CSDFT are to approach the description of charge, spin and electronic excitation transfer reactions. In this work, however, we will only focus on hole transfer reactions and leave to future developments the other types of transfer phenomena. Although FDE was successfully formulated also to model charge transfer reactions [91, 92], including photoinduced ones [111], its applicability is limited to only those transfers that occur from two (or more) non-covalently bonded molecules. That is, FDE cannot be applied if a transfer occurs between regions of the same molecule. CSDFT cures this deficiency by allowing the user to construct diabatic states for transfer reactions of embedded molecular species.

In the following, we begin by explaining the theory behind CSDFT, including details of the implementation (e.g., we assess the effect of employing two different population analyses in the definition of the CDFT constraining potential). We also address the setup and computation of superexchange couplings through a Löwdin

orthonormalization of diabatic states generated with CSDFT. We then apply CSDFT to explore and quantify the effect of the phosphate linkers in DNA hole conduction – a simulation that was simply intractable before.

3.2 Theory

KS-DFT [53] relies on a one-to-one mapping of electron densities on to a set of noninteracting electrons, also known as the KS system, whose single determinant wavefunction is built from a set of Kohn–Sham orbitals, $\{\phi_i\}$. The KS orbitals are found by locating the minimum of the DFT Lagrangian

$$\mathcal{L}_{\mathrm{DFT}}\left[\rho\right] = E_{\mathrm{HK}}\left[\rho\right] + \int v_{\mathrm{ext}}(\mathbf{r})\rho(\mathbf{r})\mathrm{d}\mathbf{r} - \mu \left[\int \rho(\mathbf{r})\mathrm{d}\mathbf{r} - N\right], \qquad (3.1)$$

in which the Hohenberg–Kohn (HK) functional is partitioned into

$$E_{\mathrm{HK}}\left[\rho\right] = T_{\mathrm{s}}\left[\rho\right] + E_{\mathrm{H}}\left[\rho\right] + E_{\mathrm{xc}}\left[\rho\right]. \qquad (3.2)$$

In the above, the electronic Coulomb repulsion energy (E_{H}), the noninteracting kinetic energy (T_{s}) and exchange–correlation energy (E_{xc}) functionals are introduced. By imposing $\mathcal{L}_{\mathrm{DFT}}\left[\rho\right]$ to be stationary, the KS equations are recovered [88].

3.2.1 Lagrangians for FDE and CDFT

Let us introduce two additional auxiliary Lagrangian expressions, one defining the Frozen Density Embedding (FDE) flavor of subsystem DFT, and the other defining the so-called Constrained DFT (CDFT). The combination of these two Lagrangians will yield the working equations of CSDFT.

FDE Lagrangian

In FDE, the total electron density is given by $\rho(\mathbf{r}) = \sum_I^{N_S} \rho_I(\mathbf{r})$, with $\{\rho_I\}$ being the set of subsystem electron densities. The energy functional is calculated as a sum of subsystem energies, with the addition of a nonadditive component that accounts for the communication between all subsystems. The electronic populations of each subsystem are constrained to integrate to a set number, which is driven by the orbital occupancy in the fragment. Thus, the FDE Lagrangian differs from $\mathcal{L}_{\text{DFT}}[\rho]$, featuring additional constraints [55, 121]:

$$\mathcal{L}_{\text{FDE}}[\{\rho_I\}] = \sum_I^{N_S} E_{\text{HK}}[\rho_I] + E_{\text{HK}}^{nad}[\{\rho_I\}] +$$
$$+ \int v_{ext}(\mathbf{r}) \times \left[\sum_I^{N_S} \rho_I(\mathbf{r})\right] \mathrm{d}\mathbf{r} - \sum_I^{N_S} \mu_I \left[\int \rho_I(\mathbf{r})\mathrm{d}\mathbf{r} - N_I\right]. \qquad (3.3)$$

The last term in the above equation, assures particle conservation for each subsystem density with μ_I being the subsystem chemical potential. $E_{\text{HK}}^{nad}[\{\rho_I\}]$ is the nonadditive HK functional, which takes the form

$$E_{\text{HK}}^{nad}[\{\rho_I\}] = T_{\text{s}}^{nad}[\{\rho_I\}] + E_{\text{H}}^{nad}[\{\rho_I\}] + E_{\text{xc}}^{nad}[\{\rho_I\}], \qquad (3.4)$$

with $F^{\text{nad}}[\rho_I, \rho_{II}, \ldots, \rho_{N_S}] = F[\rho] - \sum_I^{N_S} F[\rho_I]$.

CDFT Lagrangian

The main idea behind Constrained DFT is to bias the electronic self-consistent field procedure so that the electron density satisfies an additional artificial constraint. If such constraint can be expressed in real space as a local potential, then the CDFT

Lagrangian takes the following form,

$$\mathcal{L}_{\mathrm{CDFT}}[\rho] = E_{\mathrm{HK}}[\rho] + \int v_{ext}(\mathbf{r})\rho(\mathbf{r})\mathrm{d}\mathbf{r} + V_c\left[\int \omega_c(\mathbf{r})\rho(\mathbf{r})\mathrm{d}\mathbf{r} - N_c\right]. \qquad (3.5)$$

The first two terms are defined similarly as in Eq. (3.3) and the third is the constraint. V_c is a Lagrange multiplier, and $\omega_c(\mathbf{r})$ is the weight operator defining the constraint with N_c being the constraint value.

CDFT has been developed [49] to generate diabatic states for charge and spin transfer reactions [114]. For this, the $\omega_c(\mathbf{r})$ potential has generally been a population analysis that spans only a portion of a molecule so that charge, spin or change and spin localization is achieved [128].

3.2.2   Combining the two Lagrangians: the CSDFT method

The goal of CSDFT is to first use the FDE theory to treat the system as a collection of interacting subsystems, and second, similarly to CDFT, to apply to each subsystem (or a subset of them) a real-space constraint. This leads us to the CSDFT Lagrangian. Namely,

$$\mathcal{L}_{\mathrm{CSDFT}}[\{\rho_I\}] = \mathcal{L}_{\mathrm{FDE}}[\{\rho_I\}] + \sum_I^{N_S} V_c^I \left[\int \omega_c^I(\mathbf{r})\rho_I(\mathbf{r})\mathrm{d}\mathbf{r} - N_c^I\right] \qquad (3.6)$$

As a result of the FDE treatment, each subsystem is mapped on its own KS system with the subsystem KS orbitals given by the following set of coupled Schrödinger equations solved selfconsistently:

$$\left[\frac{-\nabla^2}{2} + v_{\mathrm{KS}}^{\mathrm{I}}(\mathbf{r}) + v_{\mathrm{emb}}^{\mathrm{I}}(\mathbf{r}) + V_c^I\omega_c^I(\mathbf{r})\right]\phi_{(i)I}(\mathbf{r}) = \epsilon_{(i)I}(\mathbf{r})\phi_{(i)I}(\mathbf{r}). \qquad (3.7)$$

where $\phi_{(i)I}(\mathbf{r})$, $\epsilon_{(i)I}$ are the molecular orbitals and orbital energies of subsystem I. In Eq. (3.7), $v_{\mathrm{emb}}^{\mathrm{I}}$ incorporates the interactions between subsystems and takes the

following form:

$$v_{\text{emb}}^{\text{I}}(\mathbf{r}) = \sum_{J \neq I}^{N_S} \left[\int \frac{\rho_J(\mathbf{r}')}{|\mathbf{r} - \mathbf{r}'|} d\mathbf{r}' - \sum_{\alpha \in J} \frac{Z_\alpha}{|\mathbf{r} - \mathbf{R}_\alpha|} \right] +$$
$$+ \frac{\delta T_{\text{s}}[\rho]}{\delta \rho(\mathbf{r})} - \frac{\delta T_{\text{s}}[\rho_I]}{\delta \rho_I(\mathbf{r})} + \frac{\delta E_{\text{xc}}[\rho]}{\delta \rho(\mathbf{r})} - \frac{\delta E_{\text{xc}}[\rho_I]}{\delta \rho_I(\mathbf{r})}. \tag{3.8}$$

The convergence of the set of equations in Eq. (3.7) is achieved in this work by the so–called freeze-and-thaw procedure [124, 47], which allows convergence of each subsystem density self–consistently with respect to the other subsystems.

CSDFT was implemented in a locally modified version of ADF[112] in such a way to be compatible with all the exchange–correlation functionals available (including orbital dependent functionals). The CSDFT algorithm can be summarized as follows:

1. The density matrix of subsystem I at SCF cycle n ($\mathbf{P}_I^n$) is employed to build the subsystem Fock matrix.

2. The density matrices of the other subsystems are used to construct the embedding potential, $v_{\text{emb}}^{\text{I}}$.

3. An initial guess of the CSDFT constraint for that subsystem is given, $V_c^I(n, 0)$, where 0 indicates the first CSDFT cycle.

4. Eq. (3.7) is solved for with $V_c^I = V_c^I(n, 0)$.

5. The CSDFT constraint $N_c^I(n, 0) = \int \omega_c^I(\mathbf{r}) \rho_I(\mathbf{r}) d\mathbf{r}$ is evaluated and compared to the given N_c^I.

6. Using a function optimizer (braketing and a golden search algorithm adapted from numerical recipes) a new value for V_c^I is determined, which is now indicated by $V_c^I(n, 1)$, and the subsystem Fock matrix is rediagonalized.

7. Steps 4–6 are repeated m times until $|N_c^I(n, m) - N_c^I| < \delta$ with δ set by the user. In our simulations we used $\delta = 10^{-12}$a.u.. Each inner CDFT cycle takes a

negligible fraction of the computational cost of building the Fock matrix. Values of m between 30 and 50 are needed on average to reach convergence for each SCF cycle. The number of CDFT iterations (i.e., m) needed are system dependent and generally decrease as the SCF procedure nears convergence. Overall, the SCF cycle is slowed down anywhere between 2 to 10 times the original timing. However, our implementation is undergoing optimizations, and we expect to improve upon such timings in future releases of the code.

8. A new density matrix, $\mathbf{P}_I^{n+1}$, is found. m is set to 0, and $\mathbf{P}_I^{n+1}$ is used again in Step 1 until the SCF reaches convergence.

9. Once convergence is achieved for subsystem I, its density matrix is frozen and the above steps are repeated for the SCF of subsystem $I + 1$.

3.3   Computational Details

All computations have been carried out with a locally modified version of ADF 2015[112]. The GGA functional PBE[93] for the exchange–correlation along with TZP basis set were employed in all computations. When carrying out a CSDFT calculation we used the PBE/PW91K/TZP level of theory (e.g., PBE for exchange–correlation, PW91k for the nonadditive kinetic energy, and the TZP basis set). A series of three freeze–thaw cycles were used to bring the CSDFT subsystem densities to selfconsistency. The DNA geometries were generated with the NAB tool of the AMBERTOOLS package[13].

As we have indicated in the theory section, the CDFT constraining potential, $\omega_c(\mathbf{r})$, is defined differently depending on the population analysis employed. In this work, we make use of the newly formulated Yukawa population analysis[32]. As such a population analysis has never been employed before in CDFT computations, we first analyze its suitability for describing diabatic states for hole transfer. The

unnormalized Yukawa population analysis function is defined by[32]:

$$\mathcal{P}_i(r) = \eta_i \frac{\exp(-2r)}{r^3}, \tag{3.9}$$

where the size–adjustment parameter η_i takes values of 0.3 for hydrogen and 1 for all other elements (all quantities in atomic units). r is the distance from nucleus i. This unnormalized function is then normalized as follows:

$$p_i(r) = \frac{\mathcal{P}_i(r)}{\sum_j \mathcal{P}_j(r)}. \tag{3.10}$$

In the results section, we will compare CDFT diabatic states computed with the Yukawa and the well established Becke population analysis.

3.4 Population analysis: Yukawa vs. Becke

In this section we report benchmark calculations of the performance of two different population analyses used in the definition of the $\omega_c(\mathbf{r})$ CDFT potential for the construction of diabatic states for hole transfer in two radical cation molecular systems: byphenyl (BP) and diphenylmethane (DPM). This is of particular interest, due to the fact that CDFT is dependent on the population analysis employed in defining the $\omega_c(\mathbf{r})$ potential. The population analyses are used to constrain a hole on one of the phenyl rings. We employ the widespread Becke population analysis [5] in comparison with the Yukawa population analysis [32], and as third-party monitor we compute Hirshfeld and Mulliken charge analysis. For sake of clarity, let us stress that we do not define the constraining potentials in terms of Mulliken or Hirchfield populations, as it is well-known that the former leads to inaccurate diabatic states[129] and the latter has not been implemented yet in our CSDFT code. This test shows whether Becke or Yukawa population analyses lead to physically similar diabatic states.

As the sought diabatic state is one in which one of the phenyl rings is positively charged by one excess hole, the rest of the molecule is overall neutral showing some polarization. In Figure 3.1, the considered molecules are displayed.
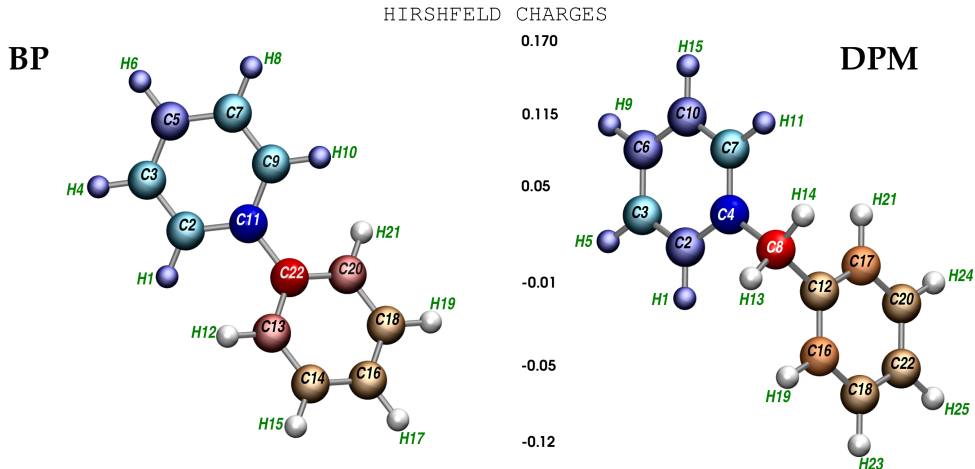
Figure 3.1: Color coated Hirshfeld atomic partial charges in BP and DPM radical cations when the positive charge is constrained to be localized on the upper phenyl rings. Blue denotes positive charges and Red denotes negative charges. Reproduced with permission from reference 99

Table 3.1, shows that both Yukawa and Becke produce similar diabatic states. Yukawa is consistent with Becke not only in the magnitude of the charge but also in the sign of the charge on each atom. In addition, in DPM the sum of atomic Hirshfeld charges for the positively constrained region is 1.0001 for both Becke and Yukawa derived $\omega_c(\mathbf{r})$ (0.9998 and 0.9999, respectively from Mulliken charge analysis). For BP, once again Becke and Yukawa produce the same overall Hirshfeld charges in the positively charged region.

Figure 3.1 displays qualitatively the Hirshfeld charges for BP and DPM. The interesting point to note in the figure is the fact that of the atoms in the constrained region (C: 2, 3, 5, 7, 9 and 11, H: 1, 4, 6, 8 and 10 for BP and C: 2, 3, 4, 6, 7 and 10, H: 1, 5, 9, 11 and 15 for DPM) the ones situated at the boundary carry the largest charge. This effect is more severe in BP than in DPM. We speculate this is because in DPM a methylene group is acting as a bridge, and its sp^3 hybridization is capable of

		Hirshfeld		Mulliken	
System	Atom	Becke	Yukawa	Becke	Yukawa
DPM	C2	0.1076	0.0807	0.399	0.372
	C3	0.0232	0.0195	0.232	0.233
	C4	0.1575	0.1614	0.363	0.288
	C6	0.0795	0.0937	0.289	0.306
	C7	0.0287	0.0233	0.308	0.297
	C8	-0.1190	-0.1081	-0.001	0.042
	C10	0.0972	0.0740	0.303	0.280
	C12	-0.0175	-0.0118	-0.045	-0.019
	C16	-0.0635	-0.0589	0.190	0.201
	C17	-0.0543	-0.0503	0.200	0.209
	C18	-0.0383	-0.0357	0.198	0.197
	C20	-0.0352	-0.0322	0.193	0.194
	C22	-0.0343	-0.0304	0.188	0.191
BP	C2	0.0522	0.0511	0.337	0.321
	C3	0.0393	0.0400	0.242	0.248
	C5	0.1082	0.1086	0.324	0.325
	C7	0.0393	0.0400	0.242	0.248
	C9	0.0522	0.0511	0.337	0.321
	C11	0.1697	0.1695	0.305	0.270
	C13	-0.0574	-0.0563	0.163	0.178
	C14	-0.0296	-0.0302	0.202	0.196
	C16	-0.0199	-0.0202	0.203	0.202
	C18	-0.0296	-0.0302	0.202	0.196
	C20	-0.0574	-0.0563	0.163	0.178
	C22	-0.0589	-0.0587	-0.248	-0.249

Table 3.1: Hirshfeld and Mulliken charge analyses of the carbon atoms belonging to the region where the hole is constrained to reside in the radical cationic diphenyl-methane (DPM) and byphenyl (BP). In the CDFT calculation, Becke and Yukawa population analysis were employed in the construction of the $\omega_c(\mathbf{r})$ potential. Atom numbers and labels from Figure 3.1. Reproduced with permission from reference 99

blocking electronic communication between the phenyl rings. Conversely, in BP the polarization produces an induction not only to the first non-constrained atom but in the atoms bonded to it.

Summarizing the above discussion, the Yukawa partition function produces diabatic states that are comparable with the ones produced with a Becke population analysis. In the following studies, we will only employ Yukawa population analysis for generating diabatic states.

3.5   Phosphate effect on hole transfer couplings in DNA.

Recently, our group has been interested in characterizing the environmental effects in hole-transfer couplings in DNA [97]. We have analyzed the effect of polarization given by the counterstrand and ribose groups on the hole transfer superexchange couplings in two DNA oligomers, using FDE for the generation of each diabatic state[97]. We concluded that the counterstrand affects hole transfer more strongly than the riboses. In the absence of a counterstrand, the riboses slightly improve hole conduction by decreasing the tunneling potential wall separating donor and acceptor.

However, in our previous study[97], as well as in all other previous studies of hole conduction in DNA [40, 41, 106, 75, 74, 76, 7, 27, 117, 119, 116, 91, 92], couplings were calculated in the absence of phosphate groups with the argument that the phosphates are far away both geographically and energetically from the region of DNA where the hole travels through (i.e., the nucleobases). There are studies that suggest the possibility of counterions strongly affecting (even "gating") the charge transfer/transport in DNA [102, 36]. In order to model such a conducting regime, phosphate groups need to be included in the quantum mechanical modeling. In this section, we decided to shed light on the effect of the phosphate groups on the superexchange couplings in

DNA by modeling two single-stranded, dry DNA oligomers: GTG and GAG.

3.5.1   Generation of diabatic states
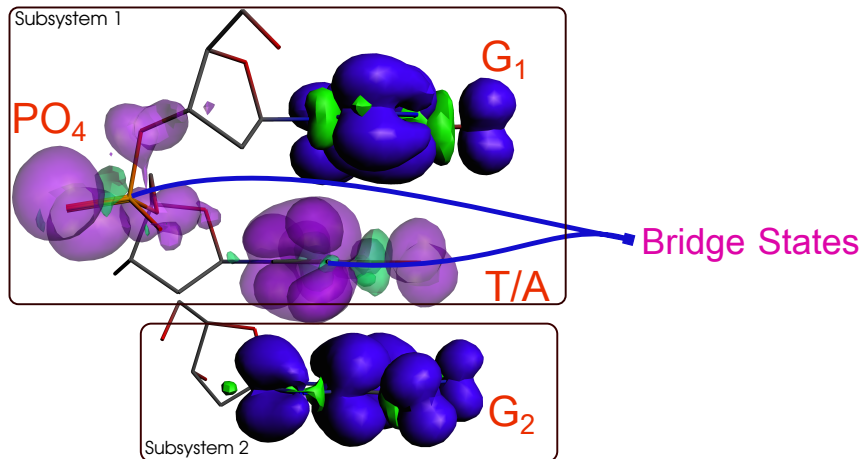
Figure 3.2: Spin densities of the four computed diabatic states for GTG and GAG systems: G_1 and G_2 feature hole localization on either guanine G_1 or guanine G_2; T or A have the hole localized on the bridge composed of thymine or adenine, respectively; PO_4 has a hole localized on the P-atom and its four surrounding Oxygen atoms. Each isosurface is the spin density of the constructed diabatic state for hole transfer in the single-stranded DNA. Given the low spin contamination in our calculations, it also represents the location of the hole. For sake of clarity, we rendered the spin density of the bridge states in a different color. Reproduced with permission from reference 99

Figure 3.2 shows the spin densities of the diabatic states considered in the CSDFT calculations. The supersystem is split into two subsystems. The first subsystem is composite, formed by guanine and adenine/thymine linked together by a PO_4 group. The second subsystem is a single guanine nucleoside (no phosphate group). CSDFT was used to calculate each diabatic state. Details of the definition of the constraining region in each diabatic state can be found in the caption of Figure 3.2.

In each computed diabat, the spin density is entirely localized on the selected atoms with insignificant spin polarization outside the selected region. The spin density in the PO_4 group is correctly mostly localized on the oxygen atoms. The HOMO

orbital computed for the PO$_4$-localized diabats has π character from the $2p_y$ orbitals of the oxygen and a small contribution from the phosphorus d, in agreement with previous studies [34]. Given the localized nature of the generated diabatic states, we conclude that the constraints are physically meaningful and can be used to understand the underlying properties of the hole transfer in DNA.

3.5.2   3- and 4-state models

We have considered three cases: two versions of a 3-state model, and a 4-state model. In the 3-state models, the hole is allowed to occupy only the nucleobases (i.e., G$_1$, G$_2$ and the bridge state T or A). In the 4-state model, in addition to the states considered in the 3-state model, we also include a state in which the hole is localized on the phosphate group. The 3-state model was considered in order to inspect how the computed couplings are affected by the presence of the PO$_4$ group.

However, we noticed that the Löwdin orthogonalization needed in Eq.(**??**) is noticeably affected by the presence of the PO$_4$-localized diabat. Therefore, we define the following models: 3_A, 3_B and 4-state models. 4-state model, contains 4 diabats before and after the Löwdin orthogonalization, 3_A-state model takes the 4-state after orthogonalization and removes the contribution to the Green operator from the diabatic state with the hole localized on the PO$_4$ group. The 3_B-state model, considers 3 diabatic states (i.e., G$_1$, G$_2$ and A/T) and performs the Löwdin orthogonalization and subsequently the calculation of the Green operator and couplings. The 4 and 3_A-state models are comparable (same orthogonalization) and allow us to access the effect of including the PO$_4$ group on the hole transfer coupling in both GTG and GAG strands.

Table 3.2 summarizes the results. These results show that the PO$_4$ group has essentially no effect on the hole transfer coupling in both GAG and GTG. We will need to perform additional computations to fully characterize these systems. For

State 1	State 2	GTG	GAG
G_1	G_2	0.006	0.008
G_1	Adenine/Thymine	0.210	0.179
G_1	PO_4	0.054	0.225
Adenine/Thymine	G_2	0.064	0.003
PO_4	G_2	0.005	0.003
Adenine/Thymine	PO_4	0.260	0.040
V_{bridge}	with PO_4	0.98	2.87
V_{bridge}	without PO_4	0.97	2.90
V_{DA}	with PO_4	7.26	11.27
V_{DA}	without PO_4	7.26	11.29

Table 3.2: Calculated $\tilde{H}$ matrix elements (in eV) and superexchange couplings (V_{bridge} and V_{DA} in meV) for GTG and GAG using the full 4-state model. V_{bridge} without PO_4 was computed with the 3_A approximation (see text). Reproduced with permission from reference 99

example, we will need to sample the nuclear degrees of freedom.

3.5.3 Comparison with earlier studies and $3_{\text{A/B}}$ state models

In order to compare CSDFT against our previous analysis [97] (which was obtained by chopping out the phosphate groups form the molecular geometry) we need to invoke the 3_B approximation (i.e., removal of the PO_4 diabat from the Hamiltonian prior to orthogonalization). We find that the GTG effective coupling for the 3_B approximation is $V_{DA} = 20.20$ meV, which compares well with the 25 meV value obtained in the prior study [97]. The couplings are not exactly the same because in our previous study we used FDE to generate the various diabatic states. Here, instead, we construct them with CSDFT. However the values are remarkably similar, showing that the CSDFT diabats are similar to the FDE ones. For GAG, the coupling obtained from the 3_B approximation is 11.55 meV which is very similar to the value obtained from the 3_A approximation. In our previous study we did not compute couplings for single stranded GAG with riboses, thus we cannot compare to it.

Inspecting again our superexchange couplings for GTG (7 meV for 3_A, and 20 meV

for 3_B), we see that they are in the same order of magnitude of the 7 meV value of Blancafort and Voityuk[7]. For GAG, Blancafort and Voityuk obtain 21 meV while we obtain 11 meV in all state models considered. We note, however, that Blancafort and Voityuk only considered the nucleobases without including in the simulation neither the riboses, nor the PO_4 groups and thus the coupling values are not expected to match quantitatively.

3.6 Conclusions

We have developed a method that combines the ability of constrained DFT to generate diabatic states for electron transfer reactions with the frozen density embedding method that provides a more computationally tractable solution to the electronic structure problem by breaking the system into interacting subsystems. We dub the resulting method CSDFT.

Computationally, our implementation of the constraining potentials utilizes the Yukawa population analysis. In two benchmark calculations we show that Yukawa population analysis produces diabatic states that are very similar to the ones produced by the commonly employed Becke population analysis.

Application of CSDFT to model DNA hole transfer allowed us to inspect the effects on hole transport caused by the PO_4 linkers present in the DNA backbone. We found that the inclusion of the phosphate in the hole transfer, is irrelevant for both GTG and GAG oligomers. Thus, we provide computational evidence that the common practice of replacing phosphates with capping groups is well justified.

Chapter 4

The eXcited Constrained DFT Method

This Chapter is adapted from the following peer–reviewed journal

- Pablo Ramos and Michele Pavanello. Low-Lying Excited States by Constrained DFT. J. Chem. Phys., accepted.

4.1   Introduction

The ability to access excited electronic states and their properties is a desirable quality of modern electronic structure theory methods. In this regard, linear-response time-dependent DFT [14] (TDDFT, hereafter) has been successfully applied to, for instance, material science [11, 120, 87] and biological systems [9, 107, 17, 109, 130, 2]. However, although it is a formally exact theory [63], TDDFT has well-documented deficiencies in the estimation of electronic excitation energies with charge-transfer and Rydberg character[22, 42] as well as in reproducing the topology of conical intersections [58]. This is due to such approximations to the exchange-correlation potential as time-locality (*i.e.*, the adiabatic approximation) and space-locality (*i.e.*, the common

employment of semilocal exchange-correlation density functionals) needed in practical implementations of the method [63].

Alternatives to TDDFT that are still based on DFT exist. Such as the constrained variational DFT method of Ziegler *et al.* [133, 131], the orthogonality-constrained DFT method of Evangelista *et al.* [25, 115], and the commonly adopted ΔSCF method and variations thereof [132, 35, 38, 54]. Although ΔSCF already provides a good estimation of excitation energies for molecular systems [54], its tendency to variationally collapse to the ground state was noted early on [132]. Such variational collapse during the ΔSCF procedure has been characterized [103] and is particularly severe in systems with dense energy spectrum near the Fermi energy. Several methods have been developed to cure this problem. The Maximum Overlap Method (MOM) [38] requires the excited ΔSCF orbitals to resemble (*via* computation of overlap integrals) the corresponding orbitals solution of the ground state SCF. The linear expansion ΔSCF method [35] requires the excited particle orbital to resemble as much as possible a reference molecular orbital. In this way, excitations can be localized on molecules when they are in contact with infinite systems (such as metal surfaces). Similarly, the local SCF (LSCF) and the improved molecular orbitals methods [28, 95] optimize a single determinant where one or more previously defined spin–orbitals are kept frozen. This assumption ensures strict orthogonality between the excited and the ground states and is often used in post-Hartree–Fock methods to more quickly converge correlation energy wrt the number of virtual orbitals [12].

Through this chapter we aim at tackling several lingering deficiencies of commonly adopted quantum chemical methods for the computation of excited states. We seek the following qualities:

1. Once an XC functional is chosen, we wish to obtain excited states energies of similar quality to the ground states ones.

2. Rate of convergence similar to the ground state SCF procedure.

3. Balanced treatment of valence and charge-transfer excitations.

4. Ability to approach complex regimes, such as conical intersections and condensed phase systems.

5. Computationally efficient access to nuclear forces and to nonadiabatic coupling vectors.

We present a constrained DFT method tailored to compute low-lying electronic excitations such that it tackles the sought qualities. We call the method eXcited Constrained DFT (XCDFT). Although the current formulation is appropriate for molecular systems, it can be generalized to solids characterized by Bloch states relatively effortlessly. XCDFT is fully *ab-initio* and does not require *ad-hoc* definitions or choice of active molecular orbitals, nor does it require the inclusion of virtual orbitals. The main idea behind XCDFT is that the virtual space of a reference ground state can be represented employing only the occupied orbitals of the reference state. Similarly to certain formulations of density functional perturbation theory that do not require the use of unoccupied bands (virtuals) [4], XCDFT resolves the space of virtuals by projection. The Fock operator is then augmented by a nonlocal and orbital dependent constraining potential that exerts a force pulling electrons into the virtual space. The strength of that potential is tuned so that exactly one electron is displaced from the occupied to the virtual space.

4.2 Theory

We use the conventional μ, ν, σ, τ labels for atomic orbital functions (AOs), i, j for occupied orbitals, and a, b for virtual orbitals. The projector onto the occupied space

of a reference "ground" state is given by

$$\hat{P}_o^g = \sum_{i_g=1}^{\text{occ}} |i_g\rangle\langle i_g|, \tag{4.1}$$

with i_g being the labels of occupied KS orbitals for the reference ground state calculation.

The main idea of XCDFT is to provide a nonlocal potential pulling electrons into the virtual space. We can construct a Fock matrix for the excited state calculation as follows:

$$\mathbb{F} = \mathbb{F}_{\text{bare}} + V_c \mathbb{W}_c, \tag{4.2}$$

with

$$(W_c)_{\mu\nu} = \langle\mu|\hat{1} - \hat{P}_o^g|\nu\rangle, \tag{4.3}$$

and $\mathbb{F}_{\text{bare}}$ being the unmodified Fock matrix. The occupied orbitals resulting from solving the mean field problem with the Fock matrix in Eq. (4.2) are denoted by $|j_e\rangle$.

The Lagrange multiplier, V_c is chosen so that there is exactly one electron in the virtual space of the ground state reference. Namely,

$$1 = \sum_{j=1}^{\text{occ}} \langle j_e|\hat{1} - \hat{P}_o^g|j_e\rangle \equiv \text{Tr}\left[\mathbb{W}_c\mathbb{D}\right] = N_e - \sum_{i,j=1}^{\text{occ}} \langle j_e|i_g\rangle\langle i_g|j_e\rangle. \tag{4.4}$$

Where we have introduced the density matrix, $\mathbb{D}$, in the AO representation.

We can cast XCDFT in a Lagrangian formalism. Namely,

$$\mathcal{L}_{\text{XCDFT}}[\mathbb{D}] = E_{\text{HK}}[\mathbb{D}] + \int v_{ext}(\mathbf{r})\rho[\mathbb{D}](\mathbf{r})\mathrm{d}\mathbf{r} + V_c\left[\text{Tr}\left[\mathbb{W}_c\mathbb{D}\right] - N_c\right], \tag{4.5}$$

where the electron density is considered to be a functional of the density matrix, $\mathbb{D}$. The XCDFT optimization involves ensuring the $\mathcal{L}_{\text{XCDFT}}$ is stationary wrt variations

in the density matrix, $\mathbb{D}$, and the XCDFT Lagrange multiplier, V_c. The first term on the rhs on Eq. (4.5) is given by,

$$E_{\mathrm{HK}}\left[\mathbb{D}\right] \equiv E_{\mathrm{HK}}\left[\rho\right] = T_{\mathrm{s}}\left[\rho\right] + E_{\mathrm{H}}\left[\rho\right] + E_{\mathrm{xc}}\left[\rho\right], \tag{4.6}$$

the second term is the interaction with the external potential, the third term is the constraint that imposes the electronic transition to the virtual space of the reference ground state and is defined in Eq. (4.4). If the XCDFT Lagrangian is differentiated with respect to number of electrons undergoing the ground-to-excited state transition (*i.e.*, N_c), considering $E[\rho] = E_{\mathrm{HK}}[\rho] + \int v_{ext}(\mathbf{r})\rho(\mathbf{r})\mathrm{d}\mathbf{r}$, the following condition is derived:

$$-\frac{\delta E[\rho]}{\delta N_c} = V_c. \tag{4.7}$$

Thus, V_c is the work needed to pull one electron from the occupied orbital space of the reference ground state to its virtual space and can be regarded as the first excitation energy. In the results section we will compare excitation energies computed from energy differences as well as from V_c.

4.2.1 Relation to the ΔSCF method

In ΔSCF, the variational problem is carried out with a non-Aufbau occupation of the molecular orbitals. Specifically, throughout the SCF procedure, the occupation of a selected occupied MO (typically the HOMO) is set to zero, and simultaneously the occupation of a virtual orbital (typically the LUMO) is set to one.

To understand how XCDFT and ΔSCF are related, we start by expressing the non-Aufbau occupation via an auxiliary system that is computed according to the Aufbau occupations but the occupied orbital energies are modified in such a way that they generate the wanted ΔSCF occupations. In doing so, we introduce an auxiliary

potential, capable of achieving the needed orbital energy shift. Namely,

$$\hat{v} = s|\text{LUMO}\rangle\langle\text{LUMO}|, \tag{4.8}$$

where s is the energy shift. Inspection of the potentials in Eq. (4.8) and Eq. (4.3) reveals that they are equivalent if $V_c = s$ in some limiting cases. Specifically, when systems have well separated orbital energies (including, but not exclusively, the HOMO–LUMO gap). In systems where the KS energy spectrum is dense, ΔSCF typically does not converge or collapses back to the original state (ground state), while XCDFT is expected to converge in almost all cases.

4.3   Computational Details and Implementation

We have implemented XCDFT in a locally modified copy of ADF (version ADF 2017[3]). The XCDFT code relies on the previously implemented Constrained DFT (CDFT) code by us [99], and handles the SCF procedure in exactly the same way (see the flow chart in Figure 4.1). At each SCF cycle, the Lagrange multiplier, V_c, is obtained so to satisfy the constraint (*i.e.*, exactly one electron resides in the virtual space of the reference ground state). Usually, the number of XCDFT nested iterations needed to reach convergence for each SCF cycle decreases as the SCF procedure nears selfconsistency.

This work comprises of two parts: benchmarking and applications. For the first part, we calculate the excitation energies of a test set of organic molecules (see Table 4.1) using XCDFT, ΔSCF, TDDFT. In all computations, the BLYP, PBE, PBE0, B3LYP and M06-2X exchange–correlation functionals were employed alongside a TZP triple-ζ Slater-Type Orbital basis set. We set an SCF convergence criterion of 10^{-6} for all calculations. The XCDFT convergence threshold, stepsize, and initial multipliers inside the nested XCDFT cycle, were 10^{-9}, 0.2 and -0.3 respectively for all systems

considered.

The applications section is divided in two subsections. First, the photoisomerization of azobenzene is analyzed by computing a relaxed scan from the trans to cis structures. This scan is achieved by using the B3LYP XC functional along with the def2-TZVP basis set as implemented in the ORCA program. At each optimized geometry a vertical excitation energy is obtained with all methods described above. Second, the solvation effects in the first excitation energy of benzaldehyde are analyzed using TDDFT, XCDFT and ΔSCF. The employed structure is taken from a molecular dynamics simulation in which the Amoeba force field[59, 94].

The evaluation of electronic couplings between the states is carried out at the GGA level using the ELECTRONTRANSFER module of ADF [92] in this way (hybrids are not yet implemented in ELECTRONTRANSFER): BLYP functional was used when the XCDFT states were obtained by B3LYP and BLYP functionals; and the PBE functional was used when PBE, PBE0 and M06-2X functionals were employed. This strategy was implemented successfully before [98].

4.4 Benchmark of XCDFT excitation energies

To asses the quality of XCDFT excitation energies, we turn to a benchmark set composed of 15 organic molecules (from aliphatic chains to DNA nucleobases) [108]. Before considering the energy values, we first confirmed that XCDFT could reproduce the character of the excitation. Table 4.1, reports the transition type of the excitation and the character involved in the excitation. We find that almost all excitations correspond to HOMO–LUMO transitions (the energy levels may be degenerate and result in mixed excitations) with the exception of tetrafluoroethylene, which features a HOMO to LUMO+2 transition. We confirmed that XCDFT reproduces the overall character of the excitations in Table 4.1 which are taken from the literature [101, 108,
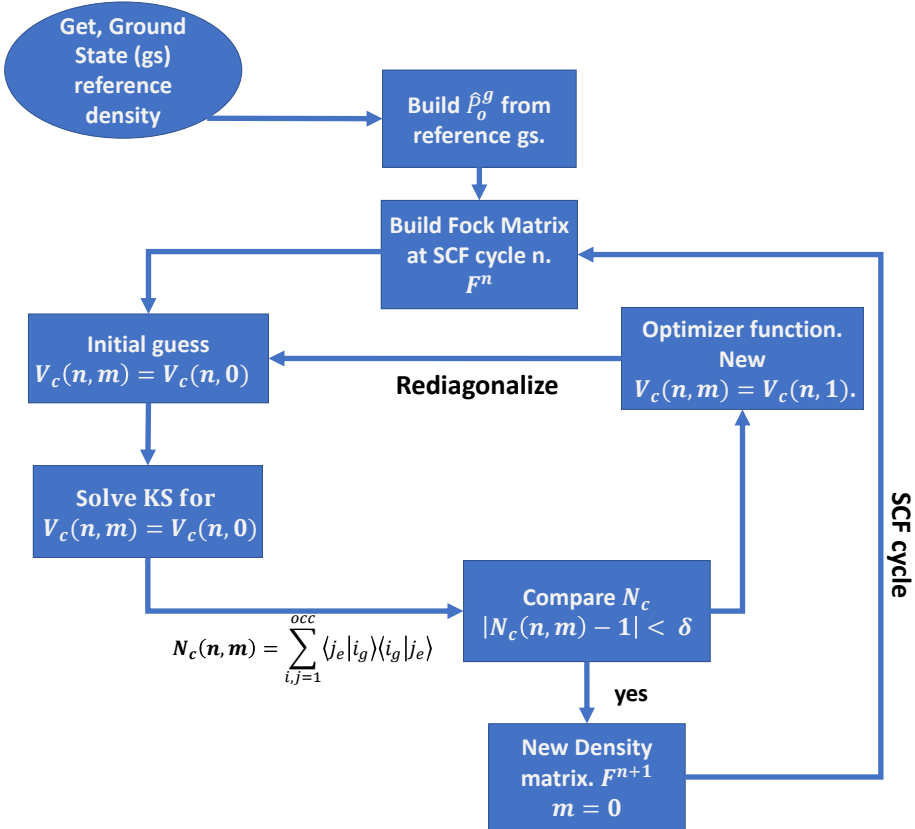
Figure 4.1: Diagram of the XCDFT algorithm implemented in ADF[3].

67, 44, 29, 135].

Label	System	Transition type	Character
1	Ethylene	$\pi \to \pi^*$	Single Orbital
2	Tetrafluoroethylene	$\pi \to 3s$	Single Orbital
3	Isoprene	$\pi \to \pi^*$	Mixed
4	1,3-Butadiene	$\pi \to \pi^*$	Mixed
5	Formaldehyde	$n \to \pi^*$	Single Orbital
6	Propanamide	$n \to \pi^*$	Single Orbital
7	Acroleine	$n \to \pi^*$	Single Orbital
8	Thiophene	$\pi \to \pi^*$	Mixed
9	Pyrrole	$\pi \to 3s$	Single Orbital
10	Benzene	$\pi \to \pi^*$	Mixed
11	Naphthalene	$\pi \to \pi^*$	Mixed
12	Pentacene	$\pi \to \pi^*$	Mixed
13	Benzaldehyde	$n \to \pi^*$	Single Orbital
14	Cytosine	$\pi \to \pi^*$	Single Orbital
15	Adenine	$\pi \to \pi^*$	Single Orbital

Table 4.1: Nature and main orbital transition of the first electronic excitations for all the systems considered in this work.

In Figure 4.2, we report the absolute error of the obtained excitations with respect to benchmark data. The bar colors are organized by XC functional employed in the calculations. Overall, we notice a satisfactory performance of XCDFT which recovers the benchmark excitation energy values to within 1 eV for most systems except isoprene, butadiene and to some degree ethylene and benzene. Low-lying excitations of these dienes are problematic for methods including only single excitations due to their sizable double excitation character [58] a feature which cannot be reproduced by linear response semilocal TDDFT [64, 24] or by the CI method when it is truncated to the singles (CIS). In terms of the excitation energies, the addition of exact exchange in the XC functional is beneficial for XCDFT and it is so on average across the entire test set. The M06-2X functional stands out and its behavior will be discussed further later.

All XC functionals yield XCDFT excitation energies in reasonable agreement with

the benchmark for system with heteroatoms (systems 5, 8, 13), aromatic rings and DNA nucleobases (systems 12, 8, 9, 14 and 15).

Focusing on the values from the orthogonalized XCDFT (OXCDFT), on average we find that the absolute errors slightly decrease compared to XCDFT. For instance, in the case of PBE0 the orthogonalization procedure improves upon the XCDFT excitation energies. However, if the overlap between ground end XCDFT excited state is numerically high (specifically higher than 0.4) we notice that the excitation energies become severely overestimated. We find this peculiarity in benzene and pyrrole systems (systems 9 and 10). As benzene exemplifies a class of excitations (*i.e.*, excitations of mixed character), we further dwell on this system in the next section aiming at uncovering any critical property of XCDFT.

Complementary to the above discussion, we also compare the numerical values of the Lagrange multiplier, V_c, as a measure of the excitation energy. V_c from GGA functionals tends to underestimate the excitation energies, while V_c from hybrid functionals is more accurate. In the next section, we will show that V_c should yield more reliable excitation energies than energy differences evaluated with the corresponding KS Slater determinants.

Figure 4.2 also shows that ΔSCF is unable to compute the excited states for tetrafluoroethylene and acroleine due to variational collapse to the ground state. For the other systems, ΔSCF behaves similarly to XCDFT. Specifically, ΔSCF deviates from the benchmark for the diene systems and benzene. While XCDFT is capable of computing almost all of the systems for which ΔSCF variationally collapses.

We also notice that when employing the M06-2X functional in XCDFT calculations of tetrafluoroethylene, acroleine and pyrrole, the character of the S_1 state differs from the one computed with the other functionals. We attribute the large XCDFT energy deviation in Figure 4.2 to this incorrect S_1 symmetry. For Tetrafluoroethylene, for example, the M06-2X excitation character is HOMO–LUMO while for the other
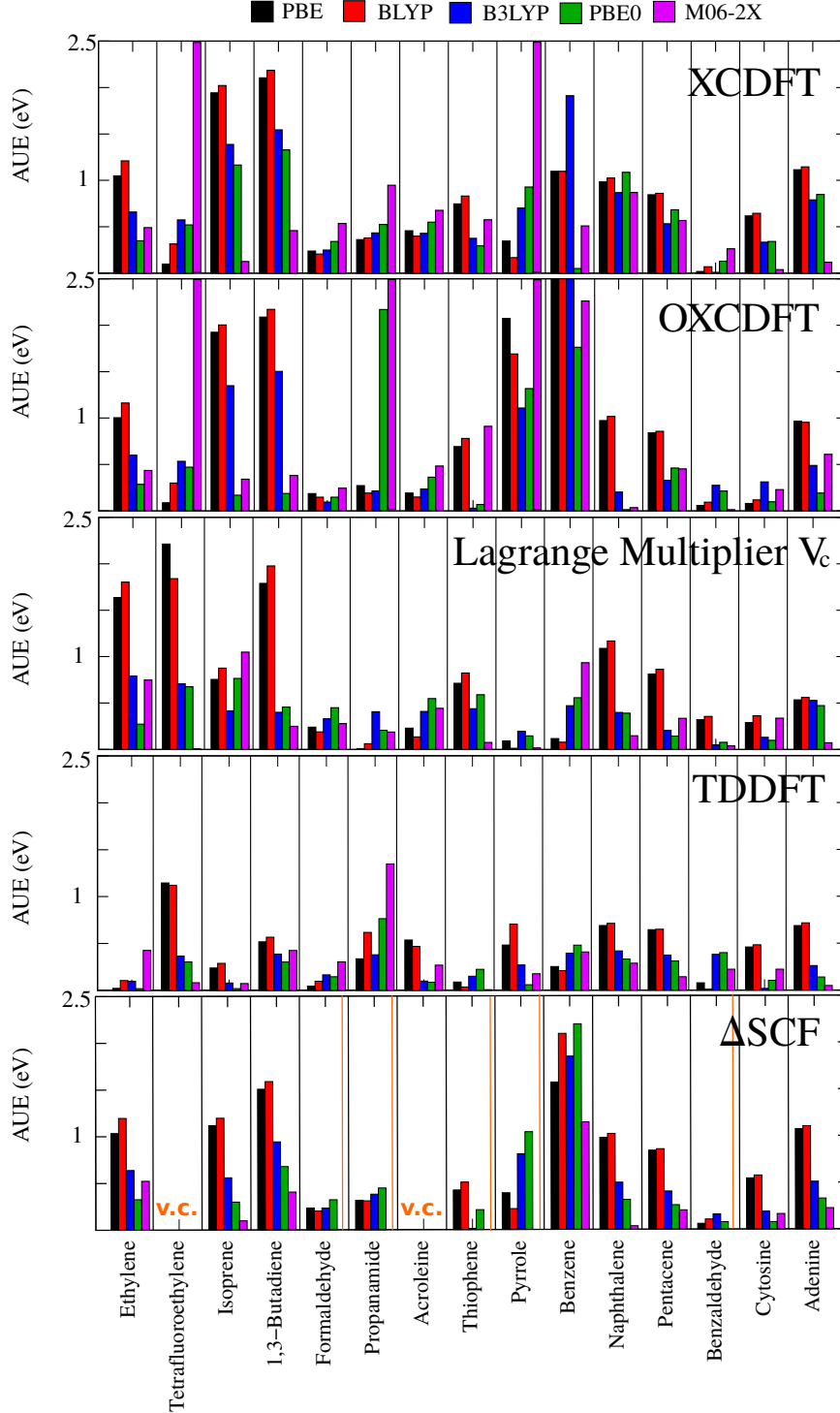
Figure 4.2: Absolute errors for all excitations evaluated with XCDFT, OXCDFT, Lagrange multiplier (V_c), TDDFT and ΔSCF. The vertical orange lines and v.c. indicate that ΔSCF has variationally collapsed to the ground state.
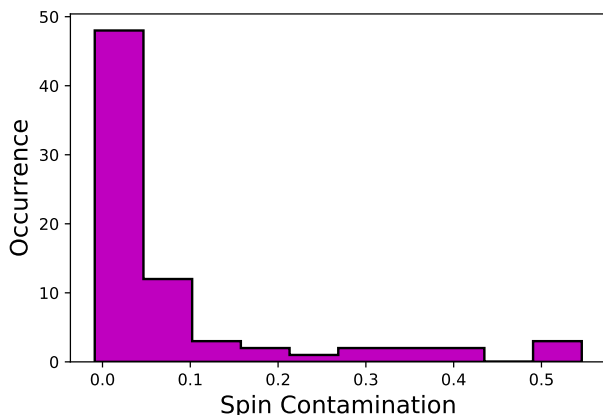
Figure 4.3: Histogram collecting the spin contamination for all XCDFT calculations. On the x-axis, deviation from 0 indicates spin contamination. The cases showing high spin contamination (values around 0.5) are PBE0 excitations of Pyrrole, Benzene and Naphthalene.

XC functionals is HOMO–LUMO+2.

In Figure 4.3 we report the spin contamination histogram for all the XCDFT calculations presented in this work (75 calculations in total). Spin contamination can be detrimental, and it is handled in this work by applying the approximate spin purification formula [54, 132], $E_{\text{XCDFT}}^{\text{purified}} = 2E_{\text{XCDFT}} - E_{\text{triplet}}$. From the figure we evince that spin contamination is only a marginal concern for XCDFT. However, we do notice that the spin purification formula improves the excitation energies, especially when employing hybrid functionals.

4.4.1 Benzene highlights how XCDFT and ΔSCF handle excitations with mixed character

Benzene has degenerate HOMO and LUMO orbitals. Therefore, the low-lying excitations are mixed in character. Specifically, when the B3LYP functional is employed, we obtain:

- S_1 state, B_{2u} symmetry: 50% HOMO to LUMO+1, 50% HOMO-1 to LUMO,

- S_2 state, B_{1u} symmetry: 50% HOMO-1 to LUMO+1, 50% HOMO to LUMO,

Thus, the $S_0 \to S_1$ TDDFT transition density is

$$\rho^*_{S_0 \to S_1}(\mathbf{r}) = \frac{1}{\sqrt{2}} \left[\phi_{HOMO}(\mathbf{r}) \phi_{LUMO+1}(\mathbf{r}) + \phi_{HOMO-1}(\mathbf{r}) \phi_{LUMO}(\mathbf{r}) \right], \qquad (4.9)$$

and the $S_0 \to S_2$ TDDFT transition density is

$$\rho^*_{S_0 \to S_2}(\mathbf{r}) = \frac{1}{\sqrt{2}} \left[\phi_{HOMO}(\mathbf{r}) \phi_{LUMO}(\mathbf{r}) + \phi_{HOMO-1}(\mathbf{r}) \phi_{LUMO+1}(\mathbf{r}) \right]. \qquad (4.10)$$

The above transition densities can only be achieved when the excited state wavefunction is composed by a linear combination of two Slater determinants.

For example, the $S_0 \to S_1$ transition is achieved in XCDFT by a Slater determinant where the selfconsistent procedure yields a HOMO orbital

$$\phi^{XCDFT}_{HOMO}(\mathbf{r}) = \frac{1}{\sqrt{2}} \left[\phi_{HOMO} + \phi_{LUMO+1} \right], \qquad (4.11)$$

and the HOMO-1 is given by

$$\phi^{XCDFT}_{HOMO-1}(\mathbf{r}) = \frac{1}{\sqrt{2}} \left[\phi_{HOMO-1} + \phi_{LUMO} \right]. \qquad (4.12)$$

Although it is clear that the work needed to promote 0.5 electrons from the HOMO-1 to the LUMO and from the HOMO to the LUMO+1 is indeed given by the XCDFT Lagrange multiplier V_c, the transition density (as well as the total S_1 density) are not going to reproduce the TDDFT ones. The resulting Slater determinant from Eq. (4.11–4.12) is

$$\Psi^{XCDFT}_{S_1} = \frac{1}{2} \left[\Psi_0 + \Psi^{LUMO+1}_{HOMO} + \Psi^{LUMO}_{HOMO-1} + \Psi^{LUMO,LUMO+1}_{HOMO-1,HOMO} \right], \qquad (4.13)$$

where we indicate by Ψ^a_i a Slater determinant differing from the ground state one

by the exchange of occupied orbital ϕ_i with virtual orbital ϕ_a. The excited state wavefunction in Eq. (4.13) contains the wanted excitation in the singly excited configurations, but contain also a sizable amount of the ground state Slater determinant and of a double excitation determinant.

If we consider a chromophore with 3 degeneracies in the HOMO and 3 in the LUMO the situation is essentially unchanged. The XCDFT determinant will feature a coefficient of $\frac{1}{\sqrt{6}}$ for Ψ_0 and collectively $\frac{3}{\sqrt{6}}$ for the double excitations, and $\frac{1}{\sqrt{6}}$ for one triple excitation.

Thus, we can conclude this analysis of cases featuring excitations of mixed character with the following take-home messages

1. XCDFT excitation energies will be reliable if evaluated by the Lagrange multiplier, V_c, and not by energy differences. This is because the energy associated with the XCDFT Slater determinant will be polluted by components in the ground state wavefunction as well as in double and higher excitations.

2. As the number of degeneracies increases, we expect XCDFT to progressively overestimate the excitation energy when energy evaluations with the XCDFT Slater determinant are carried out. While we expect excitation energies carried out with V_c to be more accurate.

3. Expectation values evaluated with the XCDFT Slater determinant will generally not yield accurate results. For example, we do not expect XCDFT or ΔSCF to reproduce the electron density of the excited states when these have mixed character.

4.4.2 Differential electron density analysis

We computed the real space representation of the differential electron density, $\Delta(\mathbf{r})$, that is the density difference between the excited and ground states[78, 126]. Namely,

$$\Delta(\mathbf{r}) = \rho_e(\mathbf{r}) - \rho_g(\mathbf{r}), \tag{4.14}$$

where $\rho_{e/g}(\mathbf{r})$ is the density of the excited/ground state.

Figure 4.4 depicts $\Delta(\mathbf{r})$ for an illustrative sample of the studied systems. The result is that XCDFT density differences typically resemble TDDFT ones as well as high level wavefunction calculations[126, 78], except for benzene.

From Figure 4.4, we also evince that $\Delta(\mathbf{r})$ has a significant dependence to the amount of exact exchange in the density functional. This behavior is seen in highly symmetric structures as well as in systems with high π-resonance along the structure (*i.e.*, where HF exchange can have the largest effect by removing degeneracies).

The set of acenes (benzene $\rightarrow$ pentacene) stands out with benzene being the most extreme case. For benzene, both XCDFT and ΔSCF qualitatively disagree with TDDFT. According to our analysis in the previous section, we expect benzene to present problems when XCDFT or ΔSCF wavefunctions are used to evaluate expectation values, such as the excited state electron density. Again, this is ascribed to the fact that XCDFT and ΔSCF can only represent the excited state with a single Slater determinant while excitations of mixed character would require a multireference wavefunction.

In the case of aliphatic structures (such as ethylene and isoprene), the electron density difference is less affected by the amount of exact exchange in the density functional.

Figure 4.4 also shows that XCDFT and ΔSCF yields similar but not exactly the same result. We expect the two methods to yield the same result only in the limiting
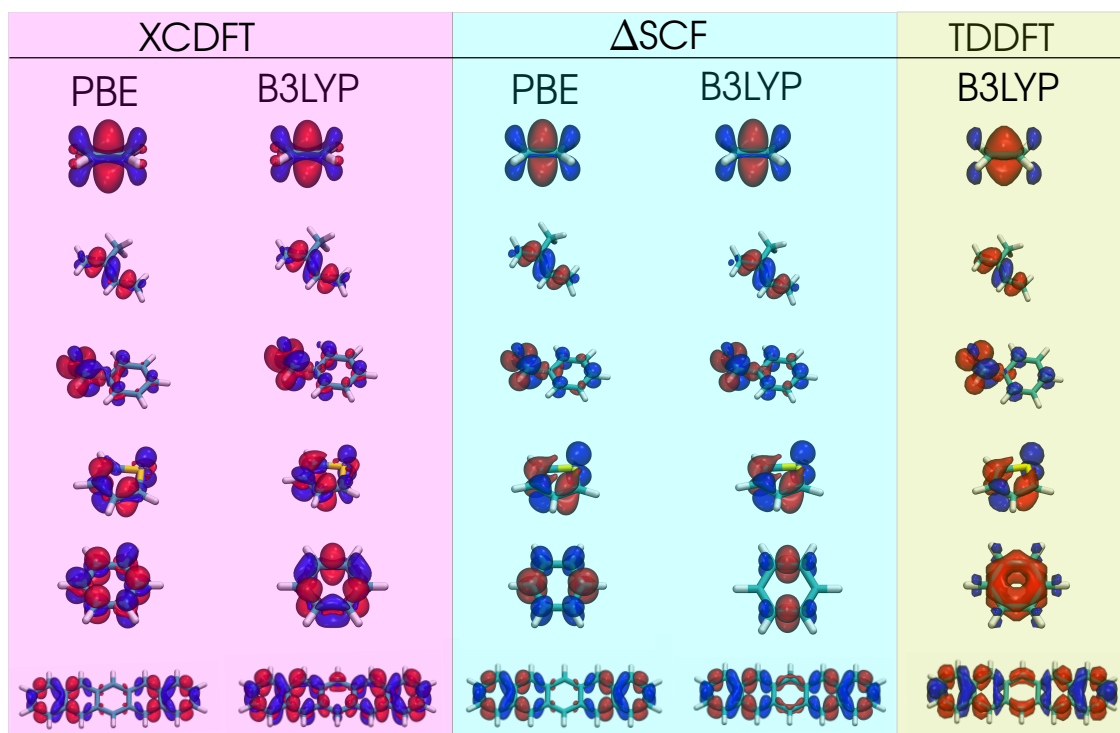
Figure 4.4: Comparison of the XCDFT (pink background) differential electron density $\Delta(\mathbf{r})$ with ΔSCF (blue background) and TDDFT (yellow background) computed with the B3LYP functional. The isosurface value taken for the surfaces was 0.003 a.u.. Figures generated with VMD [45].

case of nondegeneracy in the LUMO and HOMO levels as well as large gaps between LUMO and LUMO+1 and HOMO and HOMO-1.

4.4.3 Three parameters (p, m and d) aimed at analyzing the computed excitations

While the results in Figure 4.4 were obtained by a pointwise difference of the electron density functions of excited and ground states, we also evaluated the difference of excited and ground state density matrices in the basis of the MOs of the excited state [$i.e.$, $\{|i_e\rangle\}$ in the notation of Eq. (4.1–4.4)]. Namely,

$$\Delta_{ij} = \delta_{ij} - \sum_k \langle i_e|k_g\rangle\langle k_g|j_e\rangle. \tag{4.15}$$

Evaluating this matrix is useful because it allows us to determine if the excited state has strong orbital mixing character by inspecting its eigenvalues. Towards this goal, we borrow a metric from Ref.69, which prescribes to calculate the eigenvalues of $\Delta(\mathbf{r})$ (the eigenvalue equation $\mathbf{\Delta t}_i = \lambda_i \mathbf{t}_i$) and perform the following summation:

$$p = \frac{1}{4}\sum_j \lambda_j^2 - \lambda_j^4. \tag{4.16}$$

From the analysis of Mavros et $al.$ [69], it is concluded that charge transfer states generated with CDFT and featuring a value of $p > 0.1$ are mixed in character and will yield incorrect distance dependence in the computed electronic couplings. Although CDFT and XCDFT are very different methods and target very different constrained states, we adopt this metric p because it can single out the excitations with mixed character (such as the ones occurring in the benzene molecule). In our calculations, the p values are typically several orders of magnitude lower than 0.1, thus in Table 4.2 we report $-log(p)$ instead.

System	PBE	BLYP	B3LYP	PBE0	M06-2X
Ethylene	3.1	3.1	2.9	2.9	3.0
Tetrafluoroethylene	3.4	3.5	3.1	3.0	2.5
Isoprene	3.5	3.5	3.1	1.6	1.5
1,3-Butadiene	3.6	3.6	3.1	1.6	2.1
Formaldehyde	3.3	3.3	2.9	2.8	2.6
Propanamide	1.9	1.6	2.4	2.4	**1.1**
Acroleine	2.6	2.6	2.1	1.9	1.9
Thiophene	3.0	3.0	1.5	2.7	1.5
Pyrrole	1.9	2.0	1.5	1.6	1.5
Benzene	**1.0**	**1.0**	**1.0**	**1.0**	**1.0**
Naphthalene	3.6	3.7	**1.2**	**1.1**	**1.1**
Pentacene	4.3	4.4	1.4	**1.2**	**1.3**
Benzaldehyde	2.1	2.2	1.6	1.4	**1.1**
Cytosine	2.2	2.2	1.8	1.5	1.9
Adenine	2.3	2.3	1.3	**1.1**	1.6

Table 4.2: Computed $-\log(p)$ for the transition from ground to first excited state for all systems considered. The p values close to $p = 0.1$ threshold are given in bold font.

To make use of the computed p values, we have determined that those excitations with $-\log(p)$ values above 2.0 are strictly of single-orbital character. Below 1.5, orbital mixing starts to be noticeable. While in principle orbital mixing is not a negative characteristic of an excitation, our analysis above regarding how single reference theories like XCDFT and ΔSCF approach excitations of mixed character prompts us to become aware of when a mixed character excitation occurs. This allows us to (1) avoid using the KS determinant of the excited state for any expectation value; (2) use the Lagrange multiplier, V_c, as a more reliable estimate of the excitation energy.

Figure 4.5 displays a summary for the p parameter as a function of the XC functional employed. The figure demonstrates that when the % of HF exchange increases the parameter p becomes larger. Thus, mixed-character excitations are more likely when hybrid functionals are employed.

As pointed out by our previous analysis on benzene, excitations of mixed character introduce in the XCDFT and ΔSCF determinants components from excitations
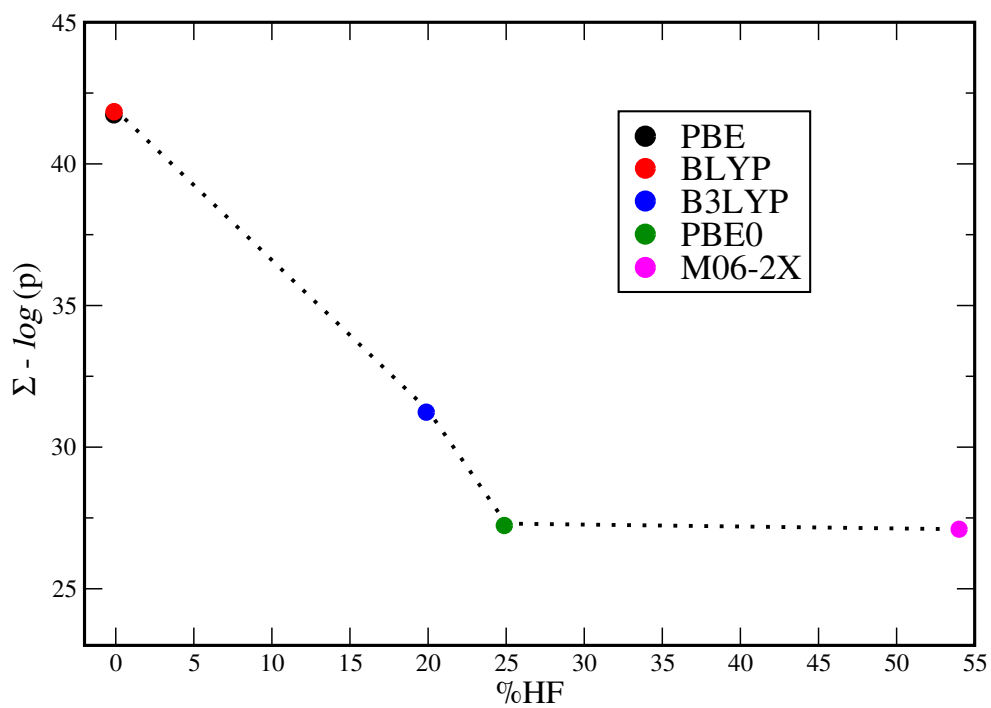
Figure 4.5: Comparison of the amount of HF, exact exchange w.r.t. the total sum of each value of the parameter $-\log(p)$ carried out for XC functional.
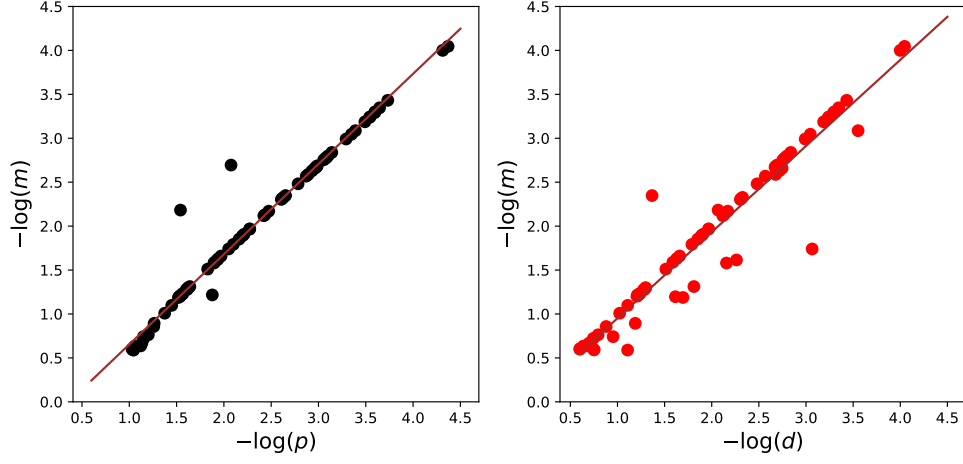
Figure 4.6: Correlation (scatter) plots of p against d and m parameters. All values in a $-\log$ scale. See Eq. (4.17) for the definition of the parameters.

higher than single. Thus, we carried out a thorough inspection of the higher-than-single excitation character (e.g., doubles, triples, ...) of the XCDFT excitations. In this regard, we consider two additional parameters: d, accounting for the amount of higher-than-single excitations; and m, accounting for mixing of the excited state with the reference ground state. The latter occurs because we do not impose orthogonality between the Kohn-Sham determinants of ground and excited states. The parameters are defined as follows:

$$
\begin{cases}
p = & \frac{1}{4} \sum_j \lambda_j^2 - \lambda_j^4, \text{ from Eq. (4.16)}, \\
m = & |\langle \Psi_0 | \Psi_e \rangle|^2, \\
d = & 1 - |\langle \Psi_0 | \Psi_e \rangle|^2 - \sum_{ia} |\langle \Psi_e | \Psi_i^a \rangle|^2.
\end{cases}
\tag{4.17}
$$

In Figure 4.6, we show correlation plots of d, m and p.

As indicated in Figure 4.6, m displays excellent correlation with p. This is a further confirmation that when the XCDFT determinant has a component on the ground state wavefunction, the excitation character is likely to be mixed. From the figure we also notice that the d vs m correlation is not as good as the p vs m.

Several points in the m vs d correlation lie below the fit–line. These are exci-

tations where the XCDFT wavefunction has significant overlap to the ground state wavefunction and low contributions from the excitations higher than single. These cases can occur if the excitation is represented as follows (or partially represented),

$$\phi_{HOMO}^{XCDFT} = a\phi_{HOMO} + b\phi_{LUMO}$$

$$\phi_{HOMO-1}^{XCDFT} = c\phi_{HOMO-1} + d\phi_{LUMO}. \tag{4.18}$$

From the above equation, it is clear that we obtain some ground state contributions while the double excitations are partially removed. We find that this is the case for Benzene when the M06-2X functional is employed featuring (from Table S1) $-\log(m) = 0.6$ and $-\log(d) = 1.1$. This is also confirmed by inspecting the excitation character of this transition (see Table 4.1).

4.5 Applications

4.5.1 Can XCDFT approach conical intersections?

With the purpose of testing the ability of XCDFT to model dynamical processes, we computed a section of the potential energy surface of ground (S_0) and excited state (S_1) of azobenzene. These states are involved in the photoisomerization process of this molecule [134, 100]. Previous studies [18, 16, 68], showed that the isomerization path from the trans-(E)-azobenzene to cis-(Z)-azobenzene occurs through rotation around the central CNNC dihedral angle, γ, (see Figure 4.7), and a conical intersection connecting S_0 and S_1 states occurs between 88° and 92°.

As shown in Figure 4.7, XCDFT recovers the correct topology at the crossing point, which we find at 90°in agreement with previous works. A closer inspection of this particular point reveals that both states S_1 and S_0 are slightly split by 0.04 eV at the crossing.
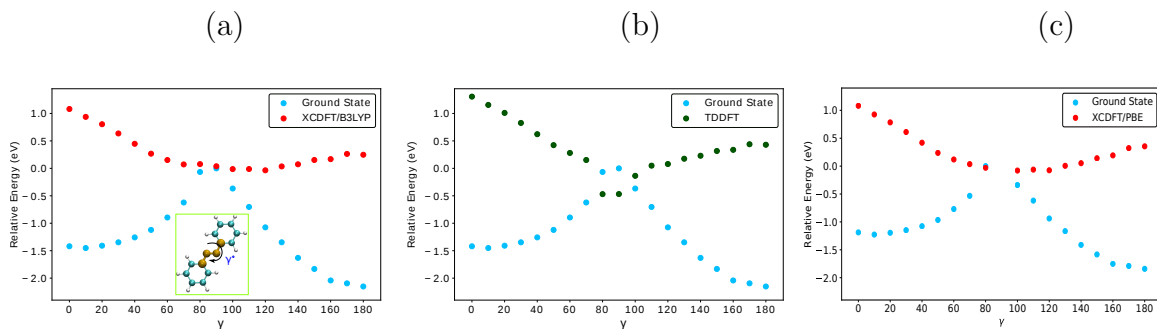
Figure 4.7: Photoisomerization of azobenzene, comparison of (a) XCDFT/B3LYP, (b) TDDFT/B3LYP and (c) XCDFT/PBE PES scans along the CNNC dihedral angle, γ. All energies are relative to the maximum energy value of the ground state occurring at 90°. ΔSCF suffers from variational collapse and thus the data is not reported (see comments in the text). All ground state constrained geometry optimizations were done with the B3LYP functional using ORCA [79].The ground state computed with the PBE functional did not converge at the crossing point.

We should point out that the ability to reproduce the correct topology of the conical intersection is moderately dependent to the amount of exact exchange in the functional. When employing PBE, for example, the geometry at the crossing could not converge in the ground state calculation. Thus the subsequent XCDFT calculation could not be carried out. For PBE, judging from the trends of ground and excited state curves, the crossing would probably have slightly incorrect topology behaving similarly to TDDFT (although not as severely) where rather than a conical intersection, a double seam is present.

Furthermore, XCDFT produces accurate excitation energies for this mechanism, the vertical excitation energy of trans-(E)-azobenzene and cis-(Z)-azobenzene are 2.40 and 2.50 eV, respectively. These are in close agreement to the experimental values and also reproduce the experiment in that the Z isomer has a lower excitation energy than E isomer. Strikingly, XCDFT is the only DFT method that within the conditions of the experiment reproduces above trend, while in the literature is found that for both TDDFT and ΔSCF the excitation energy for trans-(E)-azobenzene is higher [68]. This very good agreement with previous studies is further reinforced by low values

53

of the metrics introduced before to assess the quality of the excitation. Specifically, for all isomers, the maximum values of these metrics are: $p = 0.009$, $d = 0.09$ and $m = 0.02$.

ΔSCF, unfortunately, variational collapses along the PES scan. We also made sure that this was not a basis set dependent behavior and recomputed the ΔSCF excitations with ADF and ORCA (*i.e.*, with Slater and Gaussian type of basis sets). In both cases, ΔSCF collapses at the edges of the pathway, i.e. for γ between 0° and 50° and between 120° and 180°. However, when the Gaussian basis set is used, the range 60-110° there is no variational collapse but the excitation energies are deviated from the accepted values by over 1 eV.

4.5.2 Can XCDFT approach condensed phase systems?

We developed XCDFT hoping that it would be applicable to a wide range of processes. Solvated systems offer a particularly challenging scenario because in principle the solute and large portions of the solvent should be included in the quantum mechanical simulation. Including the solvent, however, can be a daunting task due to the sheer amount of quantum electrons that need to be accounted for in addition to the ones belonging to the solute [73]. Additional complications arise when approximate XC functionals are employed in linear response TDDFT. Artificially low-lying states of solute–solvent charge transfer character can plague the computed spectra [22, 80].

We test XCDFT for computing the solvatochromic shift in the first excitation energy of benzaldehyde when it is surrounded by 8 water molecules. In Figure 4.8 the solute–solvent system considered is depicted. XCDFT, TDDFT and ΔSCF methods were employed in two calculations each: isolated benzaldehyde (*i.e.*, *in vacuo*), and the full system (*i.e.*, benzaldehyde including the 8 water molecules). The B3LYP XC functional was employed in all calculations, because this functional provides the most accurate excitation energies for benzaldehyde for the methods employed (see Figure
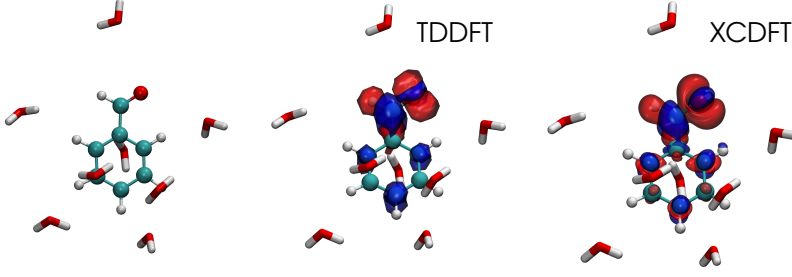
Figure 4.8: Depiction of the benzaldehyde in water system considered in this work. The differential electron density, $\Delta(\mathbf{r})$, calculated by TDDFT and XCDFT is also depicted. Figure obtained by VMD[45] with an isosurface value of 0.003 a.u for $\Delta(\mathbf{r})$.

4.2).

The differential electron density, $\Delta(\mathbf{r})$, does not show any significant difference between XCDFT and TDDFT. We find that the excitations obtained from XCDFT (both from energy differences, labelled as XCDFT, and V_c) and TDDFT are red shifted compared to *in vacuo*.

Method	E_{full}	E_{vacuo}	z_{full}
XCDFT	3.10	3.26	-0.16
V_c	3.13	3.32	-0.19
TDDFT	2.97	3.16	-0.19
ΔSCF	v.c.	v.c.	$--$

Table 4.3: Excitation energies for the composed system in Figure 4.8 with the B3LYP XC functional. E_{full} refers to the computation on the whole system, while E_{vacuo} is the energy for the isolated benzaldehyde at the same geometry of the full case. z represents the energy shift from isolated to solvated benzaldehyde. All values are reported in eV.

XCDFT and TDDFT energies differ by less than 10 %. Moreover, there is consistency in the data as the solvathochromic shift values computed by XCDFT and TDDFT are the same and can be related to available experimental data[6] where a red shift due to solvation effects is reported. This indicates that XCDFT is a suitable method for describing the electron dynamics in a condensed phase system. Conversely, ΔSCF suffers from variational collapse in both full and *in vacuo* simulations.
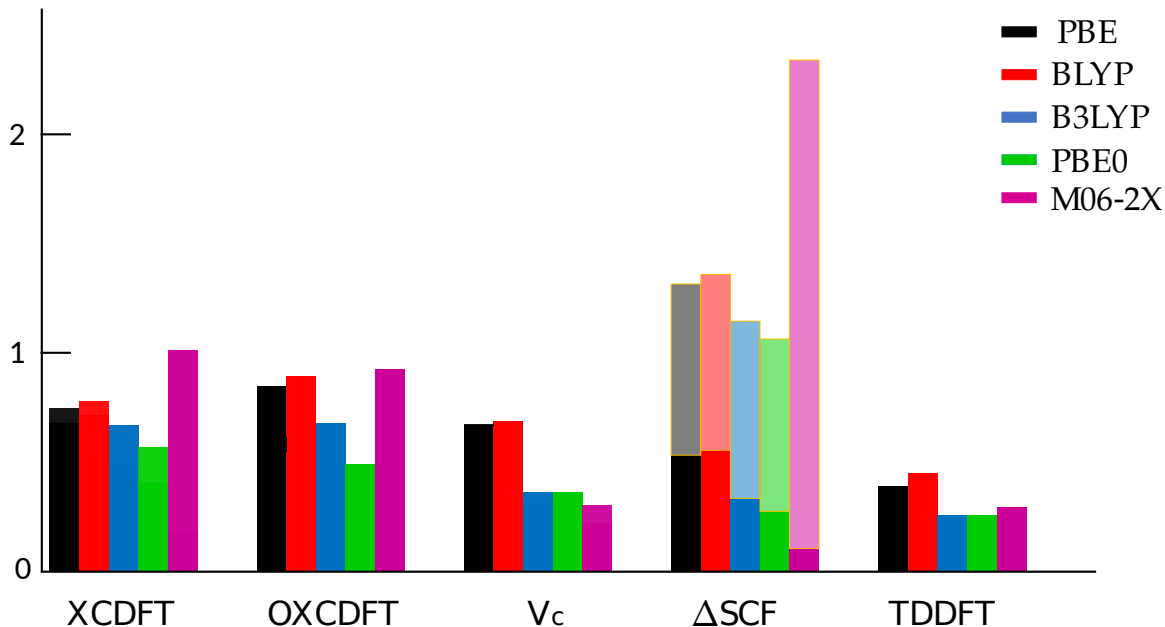
Figure 4.9: Mean unsigned error (MUE) of the excitation energy for each DFT method used in the excitation energy calculations against benchmark values. We have indicated by blurred bars the contribution to the ΔSCF errors from calculations involving variational collapse of the excited state to the ground state.

4.6 Conclusions

In sum, we have proposed XCDFT, a variational method for the computation of low-lying excited states. The method is found to produce excitation energies in quantitative agreement with TDDFT and semiquantitative agreement with benchmark calculations. We summarize this finding in Figure 4.9.

All the XCDFT variants introduced in this work (*i.e.*, XCDFT, OXCDFT and V_c) are compared in Figure 4.9 where the mean unsigned error (MUE) is also compared to TDDFT and ΔSCF. The MUE for XCDFT is typically larger that the one from TDDFT but is much smaller than ΔSCF. Unexpectedly, for several of the systems considered ΔSCF suffers from variational collapse independently of the employed functional. Variational collapse is particularly severe when the M06-2X functional is used.

We also analyze the ability of XCDFT to approach complex processes. We chose

a system featuring a conical intersection between S_0 and S_1 (azobenzene), and a solvated benzaldehyde. XCDFT is found to excellently reproduce the known trends for these systems, marking a decisive improvement over semilocal and hybrid linear response TDDFT and ΔSCF. Although we cannot claim that XCDFT will deliver good results for all systems featuring conical intersection or solvated chromophores, and despite limitations due to the single Slater determinant form of the XCDFT excited state's wavefunction, the success story outlined here for the two prototypical systems considered provides us with much needed hope, expectation and enthusiasm for further investigations of this method.

Chapter 5

Applications

This Chapter is adapted from the following peer–reviewed journals

- Pablo Ramos, Marc Mankarious, Michele Pavanello and Damien Reidel. Probing Real-Space Charge Transfer Dynamics in an Iron-Tetraphenylporphyrin Dyad on a CaF_2/Si(100) Surface. Submitted.

- Pablo Ramos, Agostino Migliore and Michele Pavanello. Charge Transfer Analysis in Peptidylglycine α-hydroxylating Monooxygenase (PHM) Enzyme. Submitted.

5.1 Fragment Orbital DFT

The fragment orbital DFT or FODFT is a computationally low-cost method to calculate electronic couplings. This is because the wavefunctions of each diabatic state are approximated by the fronteer orbitals of the isolated donor/acceptor fragments [105, 56, 86]. The underlying approximations in FODFT are that (1) the interactions between donor and acceptor have not effect on the orbital shape, (2) the coupling component related to orbitals below the fronteer is neglected (e.g. frozen core). In FODFT, the wavefunctions can be described by a single determinant of $N-1$ spin-

orbitals ϕ, where $N = N_A + N_D$ i.e. the sum of the number of electrons of the neutral donor and acceptor. These determinants are built from the KS orbitals of the noninteracting isolated donor and acceptor fragments.

$$\psi_a \approx \psi_a^{D^+A} = \frac{1}{\sqrt{(N_D - 1 + N_A)!}} \det \left(\phi_D^1 \ldots \phi_D^{N_D-1} \phi_A^1 \ldots \phi_A^{N_A} \right)$$

$$\psi_b \approx \psi_b^{DA^+} = \frac{1}{\sqrt{(N_D + N_A - 1)!}} \det \left(\phi_D^1 \ldots \phi_D^{N_D} \phi_A^1 \ldots \phi_A^{N_A-1} \right) \qquad (5.1)$$

The Hamiltonian used to calculate the CT matrix elements is the KS-Hamiltonian. Namely,

$$H_a^{KS} = \sum_{i=1}^{N_D+N_A-1} h_{a,i}^{KS}$$

$$H_b^{KS} = \sum_{i=1}^{N_D+N_A-1} h_{b,i}^{KS} \qquad (5.2)$$

where $h_{a,i}^{KS}$ are the one–particle KS–Hamiltonians for either the "a" diabat or the "b" diabat. One feature of these Hamiltonians is that they are state dependent, thus, they are made of the combination of orbitals of donor and acceptor species at the given state. The transfer integral, or coupling between states, is calculated as:

$$\psi_a \approx \psi_a^{D^+A} = \frac{1}{\sqrt{(N_D - 1 + N_A)!}} \det \left(\phi_D^1 \ldots \phi_D^{N_D-1} \phi_A^1 \ldots \phi_A^{N_A} \right)$$

$$\psi_b \approx \psi_b^{DA^+} = \frac{1}{\sqrt{(N_D + N_A - 1)!}} \det \left(\phi_D^1 \ldots \phi_D^{N_D} \phi_A^1 \ldots \phi_A^{N_A-1} \right) \qquad (5.3)$$

The Hamiltonian used to calculate the CT matrix elements is the KS-Hamiltonian. Namely,

$$H_a^{KS} = \sum_{i=1}^{N_D+N_A-1} h_{a,i}^{KS}$$

$$H_b^{KS} = \sum_{i=1}^{N_D+N_A-1} h_{b,i}^{KS} \tag{5.4}$$

where $h_{a,i}^{KS}$ are the one–particle KS–Hamiltonians for either the "a" diabat or the "b" diabat. One feature of these Hamiltonians is that they are state dependent, thus, they are made of the combination of orbitals of donor and acceptor species at the given state. The transfer integral, or coupling between states, is calculated as:

$$H_{a,b} = \langle \psi_a | H | \psi_b \rangle$$

$$\approx \langle \psi_a^{D^+A} | H_a^{KS} | \psi_b^{DA^+} \rangle$$

$$\approx \langle \phi_a^N | h_{a,i}^{KS} | \phi_b^N \rangle \tag{5.5}$$

Where N above is the fronteer orbital for D or A.

Following section are dedicated to the study of two applications, in which FODFT was used as complementary method to FDE or CSDFT methods.

5.2 Hole Transfer at NanoScale

The distance dependence of the hole transfer rate between both chromophores is evaluated when one chromophore is locally excited. In this manner, four local excitations were induced at each pyrrole group that conforms the porphyrin ring. A motif of the system can be seen at Figure 5.6, the system is made of two porphyrins at 15 Å separation between the molecular origins. Both molecules are rotated by a γ angle of 23°. Given the angle θ, two options are considered: one with the donor molecule at
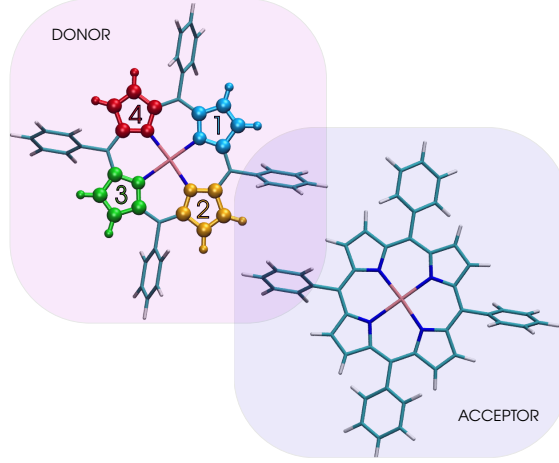
Figure 5.1: System of study, the donor molecule shows the different excitation sites.

the configuration given by the θ angle equal to 45°and one with angle of $\theta = 10°$, in both options the acceptor molecule is at the "Flat" configuration i.e. with $\theta = 10°$.

The rate of hole transfer $\Gamma(E)$ is obtained by the following equation:

$$\Gamma(E) = \frac{2\pi}{\hbar} \sum_{i \in \text{initial}} P_I(\varepsilon_i) \, f_I(\varepsilon_i - \mu_I) \, \delta(E - \varepsilon_i) \sum_{j \in \text{final}} \Theta(\varepsilon_j - \varepsilon_i) \, f_F(\varepsilon_j - \mu_F) \, |V_{ij}|^2$$

where E is the tunneling energy, P_I is the partial density of states (PDOS) of the donor at each pyrrole group, $F_{I/F}$ is the Fermi distribution function, Θ is the Heavyside step function to ensure thermodynamic irreversibility, V_{ij} is the electronic coupling between the molecular orbitals of donor and acceptor, $\mu_{I/F}$ is the Fermi level, ε the energy levels and $\delta(E)$ is the Dirac delta function.

The electronic coupling is calculated using fragment orbital DFT or FODFT. The energy levels and the PDOS are calculated individually per pyrrole site and the energy levels are computed by a single point calculation of the isolated molecule. The O3LYP exchange–correlation functional was used along with the TZP basis set for all computations.

In order to analyze the intensity of the hole rates across the energy spectrum considered, both the energy values and the electronic couplings were interpolated

using Gaussian curves. In this way, we can plot the rate of transfer as a function of the energy. In which, each peak was broaden by the following 2–dimensional smoothing function:

$$p(x, y) = e^{-[(x-x_o)^2+(y-y_o)^2]/\sigma^2}$$

where x_o and y_o are the energy levels of the donor and the acceptor within the energy range and σ is the broadening parameter which in this calculations was equal to 0.1. This 2D–Gaussian function was used for the electronic couplings, while for the energy values a one-dimensional Gaussian was sufficient.
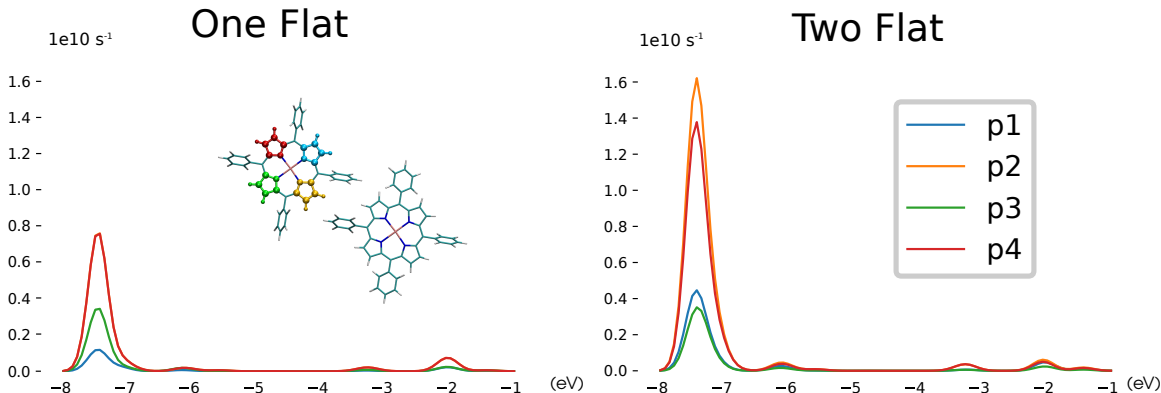
Figure 5.2: Hole transfer rates as a function of the energy for both cases in consideration. One Flat case, means that the donor molecule is a porphyrin with $\theta = 45°$, while, two Flat means the donor porphyrin has an angle of $\theta = 10°$. Note the difference in the scaling of the hole rate magnitudes between the two cases. The color distinction is given by the place of the induced excitation as previously cited in Figure 5.6. The Fermi level is represented by the dashed line.

As shown in Figure 5.2, two main restrictions are spotted. In first place, the geometry configuration plays an important role in the intensity of the calculated rate. If the θ angle has small values the rate intensity increases, specifically the rates are two times more intense when the donor chromophore has the "Flat" configuration. Secondly, an amount of energy equivalent to 2.0 eV below the Fermi level is required to peak the rate of transfer. In both situations, when the excitation is induced at

pyrrole 2 (yellow) and pyrrole 4 (red) the intensity is from 3 to 4 times higher than the rates when the pyrrole 1 (blue) and 3 (green) are excited. Both restrictions can be understood by looking at the molecular orbitals (MO) and DOS across the energy spectrum.
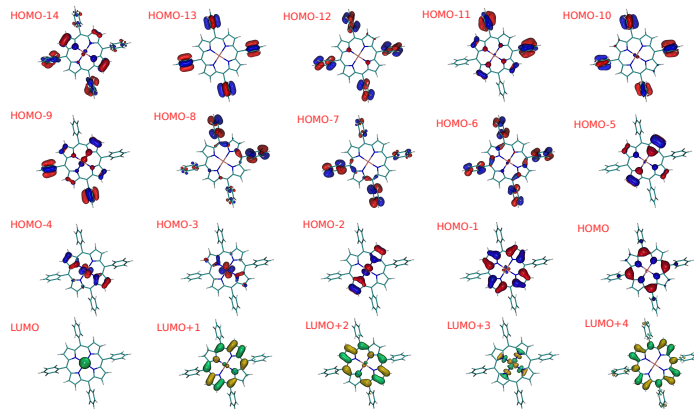
Figure 5.3: Molecular orbitals within the energy range of the donor porphyrin in the One Flat case.

Figures 5.3 and 5.4 show all MOs involved in the hole transfer within the energy range considered in the computations. The main difference between these two sets of orbitals is the electronic contribution that spreads onto the benzene radicals. When the "Flat" configuration is allow (Figure 5.4), two alternative effects to the "T" configuration occur: first, the electron density easily populate the benzene radicals as the angle is less restrictive. This effect can be seen in the virtual orbitals as well as the HOMO. On the other hand, the second effect is related to the symmetry on the population of the electron density in the benzene radicals. While in the One Flat case (Figure 5.3) the density on the benzene radicals are equally distributed, in the Two Flat case there is a non-symmetric distribution of the density. Which can explain why additional electron density can be seen at the pyrrole groups in the low energy orbitals shown in the Figures. The appreciation of the electron density in the benzene radicals might explain the difference in rate intensity. Therefore, these radicals act as bridges that reinforce the electronic communication between donor and acceptor

chromophores.
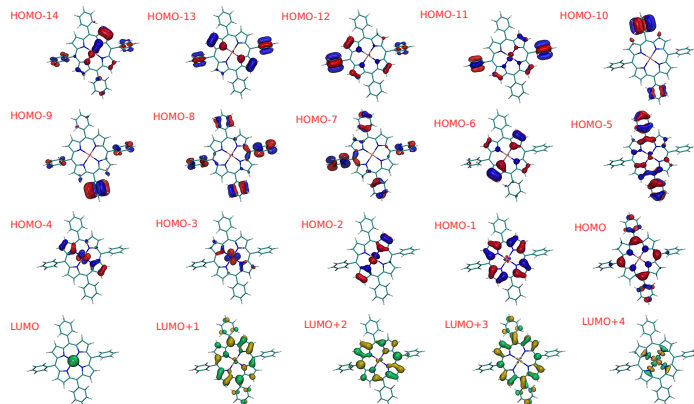
Figure 5.4: Molecular orbitals within the energy range of the donor porphyrin in the Two Flat case

Additionally, the variance in the hole transfer rates at different excited pyrrole can be easily understood by the divergence in the electron density population of each pyrrole group in every molecular orbital. As above cited, pyrrole 2 and 4 are favor by the non-symmetric "Flat" configuration. It is worth mention, that due to the coordinated bonds of the porphryrin ring with the metal center, there are more MOs where the electron density is located at pyrrole 2 and 4 within the energy range considered.

In summary, the rate of transfer is highly dependent of the excited pyrrole site, in which, the pyrrole 2 peaks the rates due to the PDOS and the closer distance separation with the acceptor site (see Figure 5.5). The benzene radicals reinforce the hole transfer rate, where the smaller the angle θ the higher the electron density population at the benzene radicals and therefore the higher the rate intensity. Finally, the energy range of 2.0 eV given by the "tip" is justify, the energy levels situated at this energy range below the Fermi level are represented with high electron density at the pyrrole groups.
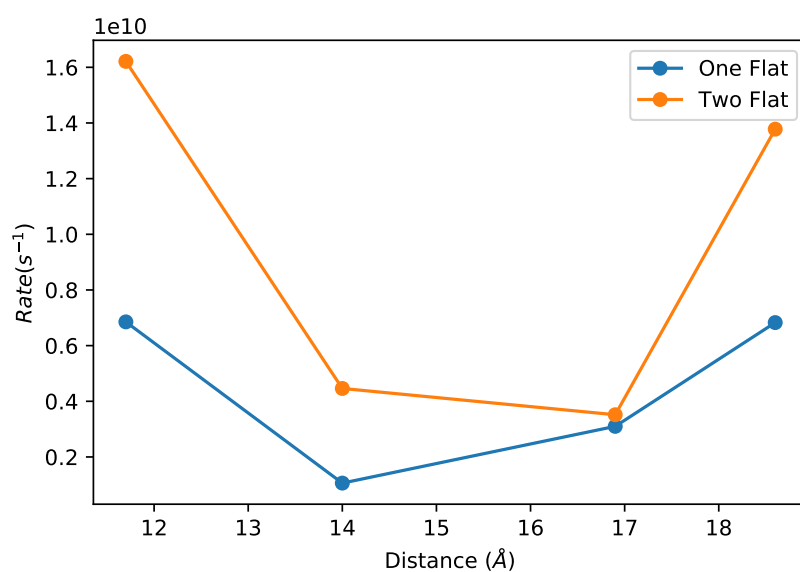
Figure 5.5: Distance dependence of the calculated rates for both cases. The distance values plotted are the separation between the molecular origin of the acceptor with the geometric center of each pyrrole group in the donor molecule. Therefore, pyrrole 1 is at 14 Å from the origin of the acceptor, pyrrole 2 at 11.7 Å, pyrrole 3 at 16.9 Åand pyrrole 4 at 18.6 Å.

5.3 Charge Transfer Analysis in peptidylglycine α-hydroxylating monooxygenase (PHM) enzyme

The Hole transfer process occurring between the two copper complexes of the peptidylglycine α-hydroxylating monooxygenase (PHM) enzyme is studied. We base our analyses on the fragment orbital density functional theory (FODFT) and frozen density embedding electron-transfer theory (FDE-ET). These analyses are done by calculating the electronic coupling between the two Cu–complexes alone (2-state model) and including two additional bridges states (4-state model) which presumably are involved in the transfer. In Figure 5.6 the total system is depicted. The Cu–complex labelled as B has a Cu(II) metal center, and is bound to three histidines. Thus, its overall charge is $+2$. The second Cu–complex is labelled as D and has a Cu(I) metal center bound to four ligands: two histidines, one methionine, and one oxo group. We have considered 3 oxidation states for the oxo group: neutral (with charge of 0), superoxo (with charge of -1), and peroxo (with charge of -2). Thus, the overall charge of the complex is $+1$, 0 or -1 depending on the oxidation state of the oxo group. There are two additional "bridge" fragments: tyrosine (labelled as C) and a propionate anion (labelled as A).

The calculations were performed with the ADF program. For the FODFT calculations, we ran a restricted single point (SP) calculation for each fragment. In all isolated calculations we used the hybrid exchange-correlation (XC) functional PBE0 along with the TZP basis set of Slater-Type Orbitals. After the isolated calculations, the couplings were determined using the PBE functional with the previously determined PBE0 orbitals.

For the FDE jobs the combination PBE/TZP/PW91K was used for the XC–functional, basis set and non–additive kinetic energy functional. The initial guess orbitals information and energetics for each fragment were borrowed from the previous
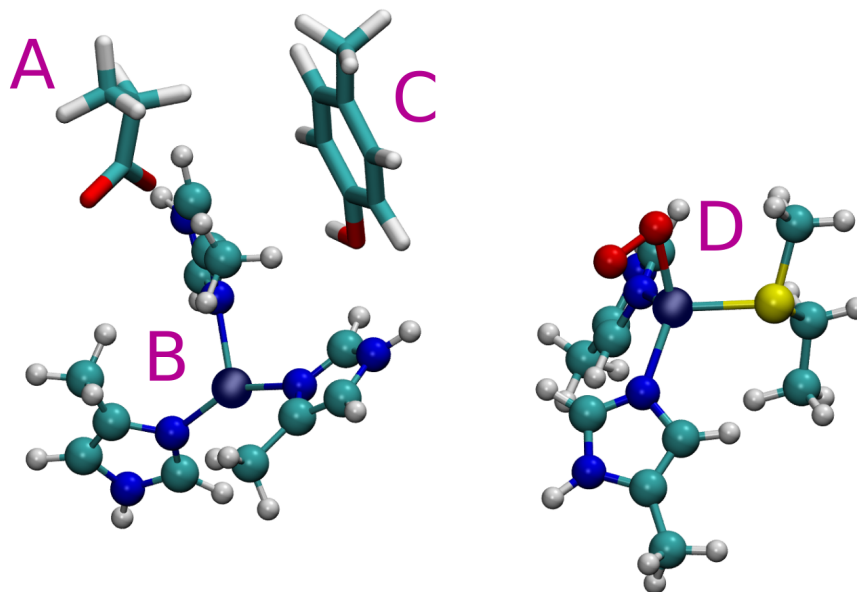
Figure 5.6: Depiction of the four fragment that composed the hole transfer system. (A) propanoate, (B) initially Cu(II) complex, (C) tyrosine, (D) initially Cu(I) complex.

SP calculations of the isolated fragments. The subsystems charge and multiplicity were carried out as described in Table 5.1 with the special treatment of fragment D, where three oxidation state were considered (i.e., oxo, peroxo and superoxo).

Fragment	Charge with hole	Spin with hole	Charge w/out hole	Spin w/out hole
A	0	doublet	−1	singlet
B	2	doublet	1	singlet
C	1	doublet	0	singlet
D (oxo)	2	doublet	1	singlet or triplet
D (superoxo)	1	singlet or triplet	0	doublet
D (peroxo)	0	doublet	−1	singlet or triplet

Table 5.1: Charge and multiplicities of each fragment with and without a hole localized on them. Fragment labels are in Figure 5.6
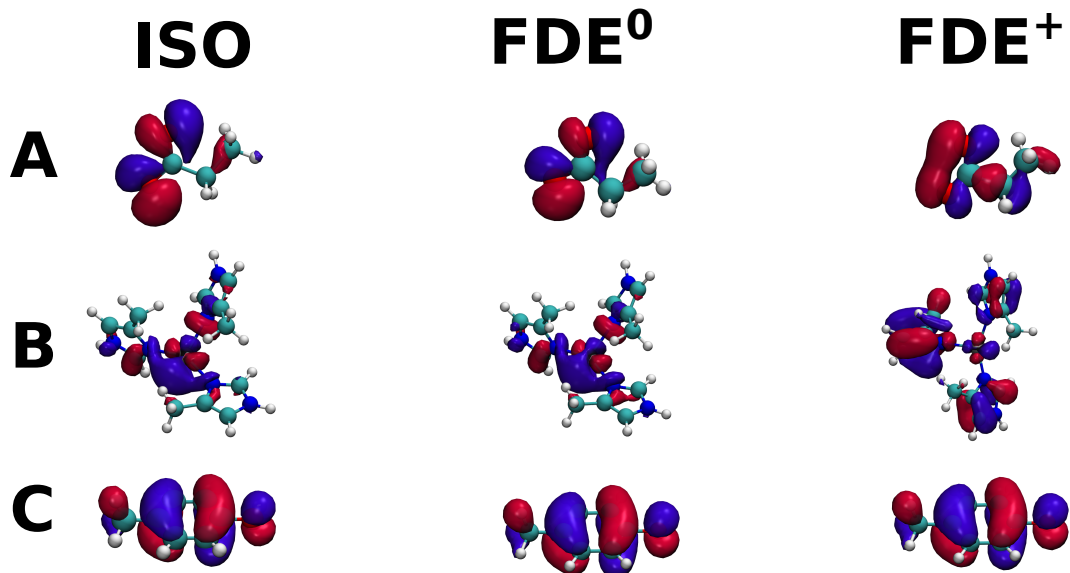
Figure 5.7: Comparison of the isolated and embedded HOMO orbitals for fragments A, B and C. In the FDE orbitals both HOMO's are depicted when the hole is in (FDE$^+$) and out (FDE^0) of the fragment. An isosurface value of 0.03 a.u. is used.[45]

5.3.1 FDE-ET results

All possible states involved in the hole transfer are shown in Figure 5.7 and 5.8 (fragment D). In all cases the HOMO orbital is illustrated when the hole is in and out of the fragment. We also compare the difference between the isolated HOMO's at PBE0 with the embedding ones ran with PBE (see FDE^0 in Figure 5.7). As it is expected the PBE HOMO's tend to be more delocalized than the PBE0 ones. Generally, PBE and PBE0 orbitals are quite similar, allowing us to compare between the FDE and FODFT electronic couplings.

Focusing on each fragment individually, we notice that when the hole is on a fragment (labelled as FDE$^+$ in Figure 5.7), fragment A (the propionate ion) has its HOMO (i.e. the beta HOMO orbital with respect to FDE^0 orbitals) orbital mainly located at the oxygen atom. The tyrosine (fragment C in Figure 5.7) has the hole spread onto the whole π region perpendicular to the molecular plane. In the donor Cu-complex (fragment B in Figure 5.7) the HOMO is located at the Cu center and

symmetrically spreads on the π orbitals of the histidine rings. Instead when the hole is away form the fragment (FDE^0 in the figure), the HOMO in fragment A acquires a node. Fragment C shows no appreciable difference when the hole is or not present. The HOMO in fragment B localizes more onto the metal center with some small contributions on the adjacent histidine ring, therefore a higher contribution from the d orbitals of Cu is witnessed compared to FDE$^+$.

For fragment D (see Figure 5.8), we have considered a number of possible oxidation states for the oxo ligand. The character of the orbitals involved is affected by the oxo ligand oxidation state. Generally speaking the HOMO of the various states of fragment D are localized on the oxo ligand. Among them there are two motifs, one involving one set of O_2-localized π^* orbitals, and the other involving the other (orthogonal) set of π^* orbitals. We also note that the most delocalized state is achieved by the neutral oxo ligand in the triplet multiplicity. An important difference between isolated and embedding HOMO's is found for the superoxo and peroxo oxidation states, the isolated HOMO's were obtained from a restricted type of calculation where not specific spin state is given, therefore the most stable configuration reached self–consistenly resembles the triplet configuration of the $+1$ case of the oxo and superoxo states (see Figure 5.8).

The calculated couplings are collected in Table 5.2. Once again, the oxidation state of the oxo ligand determines the magnitude of the couplings. Specifically, we notice that the superoxo and the peroxo oxidation states yield the largest couplings. Among the two, the superoxo oxidation state is believed to exist in the enzyme [52].

Small numerical differences in the coupling computed with the 2- and 4-state models are expected. Let us consider the following important points: Small numerical differences in the coupling computed with the 2- and 4-state models are expected. Let us consider the following important points:

1. Orthogonality: the Löwdin orthogonalization procedure will yield, even though
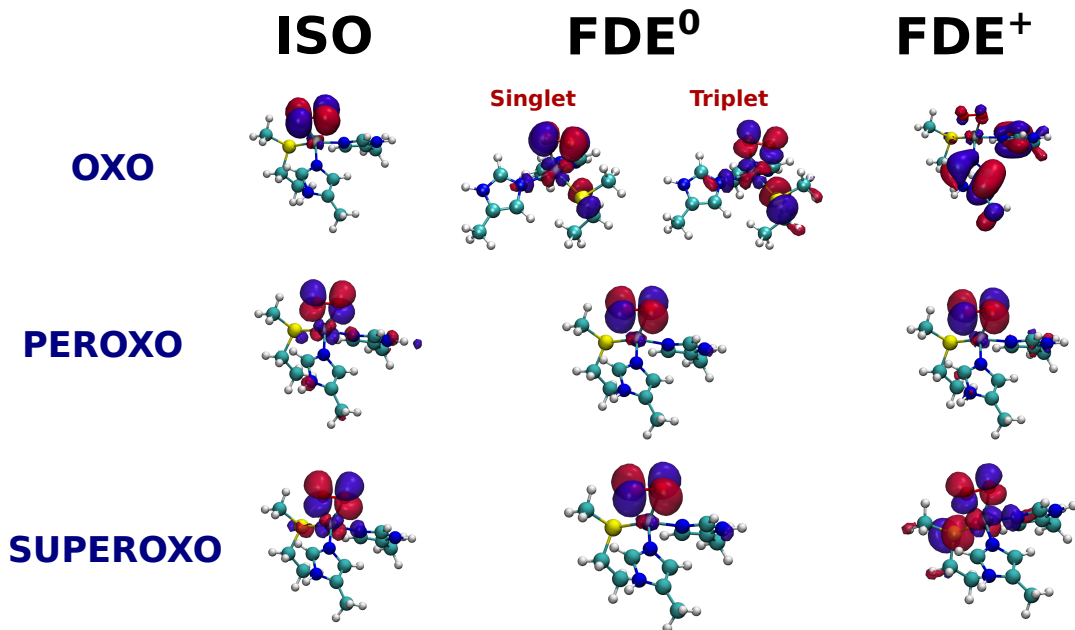
Figure 5.8: HOMO orbitals for fragment D in the three oxidation states for the O_2 group considered in the study. An isosurface value of 0.03 a.u. is used.

Oxo ligand	Active subsystems	Initial/Final spin[a]	V_{DA}	$\tilde{H}_{DA}$	V_{bridge}
$D_{(oxo)}$	4	1/2	$7.81e^{-5}$	$5.90e^{-5}$	$1.90e^{-5}$
		3/2	$5.03e^{-4}$	$3.16e^{-4}$	$1.87e^{-4}$
	2	1/2	$6e^{-6}$	$6e^{-6}$	–
		3/2	$8.17e^{-4}$	$8.17e^{-4}$	–
$D_{(superoxo)}$	4^b	2/3	$1.32e^{-3}$	$1.32e^{-3}$	$4.19e^{-6}$
	2	2/1	$7.1e^{-5}$	$7.1e^{-5}$	–
		2/3	$4.1e^{-3}$	$4.1e^{-3}$	–
$D_{(peroxo)}$	4	1/2	$3.6e^{-3}$	$3.4e^{-3}$	$1.6e^{-4}$
		3/2	$1.2e^{-2}$	$1.2e^{-2}$	$5.5e^{-5}$
	2	1/2	$1.6e^{-5}$	$1.6e^{-5}$	–
		3/2	$7.2e^{-3}$	$7.2e^{-3}$	–

a The electronic multiplicity adopted for fragment D. 1=singlet, 2=doublet, 3=triplet.

b Fragment D in its final state with singlet multiplicity did not reach self–consistency.

Table 5.2: Electronic couplings obtained for all studied cases using FDE-ET. All values are in eV.

slightly, different diabatic states in the 2- and 4-state models due to the fact that orthogonalization is applied globally and not only pair-wise.

2. State polarization: due to the self-consistent FDE procedure, all subsystems' electronic structure is polarized by the other susbsystems. Thus, the full 4-fragment system will feature slightly different local diabats from the 2-fragment system.

In our previous work [99], we noticed that imposing orthogonality globally could affect the character of far-away diabatic states. This is a side effect of the orthogonalization and highlights the difficulty of defining universal quasi-diabatic states [90, 72].

5.3.2 FODFT calculations

FODFT confirms the trends observed in the FDE-ET calculations. However, the FODFT electronic couplings are lower than the FDE-ET ones when the oxo and superoxo oxidation states and in the same order of magnitude for the peroxo state. This behavior can be explained by considering the origin of the orbitals use for the TI calculation, i.e. PBE0 orbitals which are slightly more localized that the PBE orbitals used in the FDE-ET calculations. In Figure 5.7, the HOMOs from the PBE0 calculations of the isolated fragments appear to be more localized than the PBE ones used in the FDE-ET calculations.

Due to technicalities of the FODFT program in ADF, an explicit triplet cannot be considered in FODFT calculations. Thus we decided to approximate the triplet's diabatic state in the FODFT calculations by the LUMO of the isolated fragment D when oxo and peroxo oxidation states were present. Although this is a very rough approximation, we have visually confirmed that the LUMO orbital of the isolated fragment is similar to the HOMO orbital when a triplet multiplicity is adopted in the FDE calculations. Again, FODFT follows the same trend as the FDE-ET calculations,

Oxo ligand	Active subsystems	Initial/final spin	V_{DA}	$\tilde{H}_{DA}$	V_{bridge}
	4	1/2	$1.1e^{-5}$	$1.1e^{-5}$	$4.2e^{-7}$
		3/2	$2.1e^{-5}$	$1.8e^{-5}$	$3.2e^{-6}$
$D_{(oxo)}$	2	1/2	$1.1e^{-5}$	$1.1e^{-5}$	–
		3/2	$3.5e^{-5}$	$3.5e^{-5}$	–
	4	2/1	$3.8e^{-3}$	$3.3e^{-3}$	$4.8e^{-4}$
		2/3	$2.4e^{-2}$	$2.3e^{-2}$	$4.7e^{-4}$
$D_{(superoxo)}$	2	2/1	$3.8e^{-4}$	$3.8e^{-4}$	–
		2/3	$9.3e^{-4}$	$9.3e^{-4}$	–
	4	1/2	$1.6e^{-3}$	$1.6e^{-3}$	$3.0e^{-5}$
		3/2	$3.2e^{-2}$	$2.8e^{-2}$	$3.9e^{-3}$
$D_{(peroxo)}$	2	1/2	$7.1e^{-5}$	$7.1e^{-5}$	–
		3/2	$1.1e^{-3}$	$1.1e^{-3}$	–

Table 5.3: Electronic couplings obtained for all studied cases using FODFT. All values are in eV.

and the triplet multiplicity on fragment D leads to the highest hole coupling.

Chapter 6

Conclusions

In this dissertation the candidate describes his work on the development and validation of new alternative electronic structure methods intended to model charge transfer processes. Both FDE and CSDFT methods are found to be reliable and accurate in the construction of diabatic states suitable for CT reactions. On top of that, subsystem DFT offers a way to include the environmental effects from first principles without the need to parametrize the interactions between subsystems.

The FDE-ET modeling of the hole transfer in B–DNA outlined in this dissertation showed that the effects of the ribose groups and the nucleobases in the counterstrand are opposite and different in magnitude depending on the oligomer size. Hence, the effect of the counterstrand completely overpowers any effect due to the presence of the ribose groups.

The combination of both CDFT and FDE Lagrangians provides a more computationally tractable solution to the electronic structure problem of composed systems. In this regard, CSDFT method was successfully applied to understand the impact of the phosphate groups on the hole transfer in DNA. It was found that the phosphate group is irrelevant when a hole is transfered for both GTG and GAG oligomers.

The Adiabatic version XCDFT gives accurate electronic excitations. Where the

correct behavior of various physical phenomena were achieved. The excitation energies evaluated by V_c are more accurate than direct energy evaluation. In addition, XCDFT casts itself as a versatile tool in the analysis of complex systems such as conical intersections.

The study of the two applications demonstrate not only the scale of the systems that can be tackle but also the accuracy that can be achieved by these methods, where a realistic picture of the physics behind the problems is exposed. In addition, the implementation of new routines to quantify nonadiabatic effects to the energy and the electronic coupling in composed systems would constitute a significant contribution to molecular quantum mechanics.

Bibliography

[1] Kubas Adam, Felix Hoffmann, Alexander Heck, Harald Oberhofer, Marcus Elstner, and Jochen Blumberger. Electronic couplings for molecular charge transfer: Benchmarking CDFT, FODFT, and FODFTB against high-level ab initio calculations. *J. Chem. Phys.*, 140:104105, 2014.

[2] Anna Amat, Costanza Miliani, Aldo Romani, and Simona Fantacci. Dft/tddft investigation on the uv-vis absorption and fluorescence properties of alizarin dye. *Phys. Chem. Chem. Phys.*, 17:6374–6382, 2015.

[3] Evert Jan Baerends, Tom Ziegler, A. J. Atkins, Jochen Autschbach, Donald Bashford, O. Baseggio, A. Bérces, F. Matthias Bickelhaupt, C. Bo, P. M. Boerritger, Luigi Cavallo, C. Daul, D. P. Chong, D. V. Chulhai, L. Deng, R. M. Dickson, J. M. Dieterich, D. E. Ellis, M. van Faassen, M. Franchini, A. Ghysels, A. Giammona, Stan J. A. van Gisbergen, A. Goez, A. W. Götz, S. Gusarov, F. E. Harris, P. van den Hoek, Z. Hu, Christoph R. Jacob, H. Jacobsen, L. Jensen, L. Joubert, J. W. Kaminski, G. van Kessel, C. König, F. Kootstra, A. Kovalenko, Mykhaylo Krykunov, Erik van Lenthe, D. A. McCormack, A. Michalak, M. Mitoraj, S. M. Morton, Johannes Neugebauer, V. P. Nicu, Louis Noodleman, V. P. Osinga, S. Patchkovskii, Michele Pavanello, C. A. Peeples, Pierre Herman Theodoor Philipsen, D. Post, Cory C. Pye, H. Ramanantoanina, P. Ramos, W. Ravenek, J. I. Rodríguez, P. Ros, R. Rüger, P. R. T. Schipper, D. Schlüns, H. van Schoot, G. Schreckenbach, J. S. Selden-

thuis, Mike Seth, Jaap G. Snijders, Miquel Solà, Stener M., M. Swart, D. Swerhone, G. te Velde, V. Tognetti, P. Vernooijs, L. Versluis, Lucas Visscher, O. Visser, Fan Wang, T. A. Wesolowski, E. M. van Wezenbeek, G. Wiesenekker, S. K. Wolff, T. K. Woo, and A. L. Yakovlev. ADF2017, SCM, Theoretical Chemistry, Vrije Universiteit, Amsterdam, The Netherlands, https://www.scm.com.

[4] Stefano Baroni, Paolo Giannozzi, and Andrea Testa. Green's-function approach to linear response in solids. *Phys. Rev. Lett.*, 58:1861–1864, 1987.

[5] Axel D. Becke. A multicenter numerical integration scheme for polyatomic molecules. *J. Chem. Phys.*, 88:2547, 1988.

[6] Michael. Berger, Irwin L. Goldblatt, and Colin. Steel. Photochemistry of benzaldehyde. *J. Am. Chem. Soc.*, 95(6):1717–1725, 1973.

[7] Lluis Blancafort and Alexander A. Voityuk. CASSF/CAS-PT2 study of hole transfer in stacked DNA nucleobases. *J. Phys. Chem. A*, 110:6426–6432, 2006.

[8] D. R. Bowler and T. Miyazaki. $O(N)$ Methods in Electronic Structure Calculations. *Rep. Prog. Phys.*, 75:036503, 2012.

[9] Elizabeth Brunk and Ursula Rothlisberger. Mixed quantum mechanical/molecular mechanical molecular dynamics simulations of biological systems in ground and electronically excited states. *Chem. Rev.*, 115(12):6217–6263, 2015.

[10] R. E. Bulo, C. R. Jacob, and L. Visscher. NMR Solvent Shifts of Acetonitrile from Frozen Density Embedding Calculations. *J. Phys. Chem. A*, 112:2640–2647, 2008.

[11] Young-Moo Byun and Carsten A. Ullrich. Excitons in solids from time-

dependent density-functional theory: Assessing the tamm-dancoff approximation. *Computation*, 5:9, 2017.

[12] Rosa Caballol and Jean-Paul Malrieu. Improved non-valence virtual orbitals for CI calculations. *Chem. Phys.*, 140:7–18, 1990.

[13] D.A. Case, T.A. Darden, T.E. Cheatham, III, C.L. Simmerling, J. Wang, R.E. Duke, R. Luo, R.C. Walker, W. Zhang, K.M. Merz, B. Roberts, S. Hayik, A. Roitberg, G. Seabra, J. Swails, A.W. Goetz, I. Kolossváry, K.F. Wong, F. Paesani, J. Vanicek, R.M. Wolf, J. Liu, X. Wu, S.R. Brozell, T. Steinbrecher, H. Gohlke, Q. Cai, X. Ye, J. Wang, M.-J. Hsieh, G. Cui, D.R. Roe, D.H. Mathews, M.G. Seetin, R. Salomon-Ferrer, C. Sagui, V. Babin, T. Luchko, S. Gusarov, A. Kovalenko, and P.A. Kollman. AMBER 12. University of California, San Francisco, 2012.

[14] Mark E. Casida. Time-Dependent Density Functional Response Theory for Molecules. In Delano P. Chong, editor, *Recent Advances in Density Functional Methods Part I*, pages 155–192. World Scientific, Singapore, 1995.

[15] Mark E. Casida and Tomasz A. Wesolowski. Generalization of the Kohn–Sham Equations with Constrained Electron Density Formalism and Its Time-Dependent Response Theory Formulation. *Int. J. Quantum Chem.*, 96:577–588, 2004.

[16] Alessandro Cembran, Fernando Bernardi, Marco Garavelli, Laura Gagliardi, and Giorgio Orlandi. On the mechanism of the cis–trans isomerization in the lowest electronic states of azobenzene: S0, s1 and t1. *J. Am. Chem. Soc.*, 126(10):3234–3243, 2004.

[17] Indranil Chakraborty, Samantha J. Carrington, and Pradip K. Mascharak. Design strategies to improve the sensitivity of photoactive metal carbonyl com-

plexes (photocorms) to visible light and their potential as co-donors to biological targets. *Acc. Chem. Res.*, 47(8):2603–2611, 2014.

[18] Irene Conti, Marco Garavelli, and Giorgio Orlandi. The different photoisomerization efficiency of azobenzene in the lowest nπ* and $\pi\pi$* singlets: The role of a phantom state. *J. Am. Chem. Soc.*, 130(15):5216–5230, 2008.

[19] P. Cortona. Self-Consistently Determined Properties of Solids Without Band-Structure Calculations. *Phys. Rev. B*, 44:8454, 1991.

[20] P. H. Dederichs, S. Blügel, R. Zeller, and H. Akai. Ground states of constrained systems: Application to cerium impurities. *Phys. Rev. Lett.*, 53:2512–2515, Dec 1984.

[21] Wallace D. Derricotte and Francesco A. Evangelista. Simulation of x-ray absorption spectra with orthogonality constrained density functional theory. *Phys. Chem. Chem. Phys.*, 17:14360–14374, 2015.

[22] Andreas Dreuw and Martin Head-Gordon. Single-Reference ab Initio Methods for the Calculation of Excited States of Large Molecules. *Chem. Rev.*, 105:4009–4037, 2005.

[23] Marcin Dulak and Tomasz A. Wesolowski. On the electron leak problem in orbital-free embedding calculations. *J. Chem. Phys.*, 124:164101, 2006.

[24] Peter Elliott, Sharma Goldson, Chris Canahui, and Neepa T. Maitra. Perspectives on double-excitations in TDDFT. *Chem. Phys.*, 391:110–119, 2011.

[25] Francesco A. Evangelista, Philip Shushkov, and John C. Tully. Orthogonality Constrained Density Functional Theory for Electronic Excited States. *J. Phys. Chem. A*, 117(32):7378–7392, 2013.

[26] Jeffrey W. Evenson and Martin Karplus. Effective Coupling in Bridged Electron Transfer Molecules: Computational Formulation and Examples. *J. Chem. Phys.*, 96:5272–5278, 1992.

[27] Martin Felix and Alexander A. Voityuk. DFT Performance for the Hole Transfer Parameters in DNA pi Stacks. *Int. J. Quantum Chem.*, 111:191–201, 2011.

[28] Nicolas Ferré and Xavier Assfeld. Application of the local self-consistent-field method to core-ionized and core-excited molecules, polymers, and proteins: True orthogonality between ground and excited states. *J. Chem. Phys.*, 117(9):4119–4125, 2002.

[29] Franca Maria Floris, Claudia Filippi, and Claudio Amovilli. Electronic excitations in a dielectric continuum solvent with quantum monte carlo: Acrolein in water. *J. Chem. Phys.*, 140(3):034109, 2014.

[30] Georgios Fradelos and Tomasz A. Wesolowski. The importance of going beyond coulombic potential in embedding calculations for molecular properties: The case of iso-g for biliverdin in protein-like environment. *J. Chem. Theory Comput.*, 7(1):213–222, 2011.

[31] Georgios Fradelos and Tomasz A. Wesołowski. Importance of the intermolecular pauli repulsion in embedding calculations for molecular properties: The case of excitation energies for a chromophore in hydrogen-bonded environments. *J. Phys. Chem. A*, 115(35):10018–10026, 2011.

[32] Mirko Franchini, Pierre Herman Theodoor Philipsen, Erik van Lenthe, and Lucas Visscher. Accurate Coulomb Potentials for Periodic and Molecular Systems through Density Fitting. *J. Chem. Theory Comput.*, 2014. Submitted.

[33] Samuel Fux, Karin Kiewisch, Christoph R. Jacob, Johannes Neugebauer, and Markus Reiher. Analysis of Electron Density Distributions from Subsystem

Density Functional Theory Applied to Coordination Bonds. *Chem. Phys. Lett.*, 461:353–359, 2008.

[34] Benjamin Gamoke, Diane Neff, and Jack Simons. Nature of po bonds in phosphates. *J. Phys. Chem. A*, 113(19):5677–5684, 2009.

[35] Jeppe Gavnholt, Thomas Olsen, Mads Engelund, and Jakob Schiøtz. Δ. *Phys. Rev. B*, 78:075441, Aug 2008.

[36] Joseph C. Genereux and Jacqueline K. Barton. Mechanisms for DNA Charge Transport. *Chem. Rev.*, 110:1642–1662, 2010.

[37] Alessandro Genova and Michele Pavanello. Exploiting the Locality of Subsystem Density Functional Theory: Efficient Sampling of the Brillouin Zone. *J. Phys.: Condens. Matter*, 27:495501, 2015.

[38] Andrew T. B. Gilbert, Nicholas A. Besley, and Peter M. W. Gill. Self-consistent field calculations of excited states using the maximum overlap method (mom). *J. Phys. Chem. A*, 112(50):13164–13171, 2008.

[39] A.W. Götz, S.M. Beyhan, and L. Visscher. Performance of Kinetic Energy Functionals for Interaction Energies in a Subsystem Formulation of Density Functional Theory. *J. Chem. Theory Comput.*, 5:3161–3174, 2009.

[40] Ferdinand C. Grozema, Yuri A. Berlin, and Laurens D. A. Siebbeles. Mechanism of Charge Migration through DNA: Molecular Wire Behavior, Single-Step Tunneling or Hopping? *J. Am. Chem. Soc.*, 122:10903–10909, 2000.

[41] Ferdinand C. Grozema, Stefano Tonzani, Yuri A. Berlin, George C. Schatz, Laurens D. A. Siebbeles, and Mark A. Ratner. Effect of Structural Dynamics on Charge Transfer in DNA Hairpins. *J. Am. Chem. Soc.*, 130:5157–5166, 2008.

[42] Myrta Grüning, Oleg V. Gritsenko, Stan J. A. van Gisbergen, and Evert Jan Baerends. On the required shape corrections to the local density and generalized gradient approximations to the kohn–sham potentials for molecular response calculations of (hyper)polarizabilities and excitation energies. *J. Chem. Phys.*, 116:9591–9601, jun 2002.

[43] Elizabeth Hatcher, Alexander Balaeff, Shahar Keinan, Ravindra Venkatramani, and David N. Beratan. PNA versus DNA: Effects of Structural Fluctuations on Electronic Structure and Hole-Transport Mechanisms. *J. Am. Chem. Soc.*, 130:11752–11761, 2008.

[44] D. M. P. Holland, A. B. Trofimov, E. A. Seddon, E. V. Gromov, T. Korona, N. de Oliveira, L. E. Archer, D. Joyeux, and L. Nahon. Excited electronic states of thiophene: high resolution photoabsorption fourier transform spectroscopy and ab initio calculations. *Phys. Chem. Chem. Phys.*, 16:21629–21644, 2014.

[45] W. Humphrey, A. Dalke, and K. Schulten. VMD — Visual Molecular Dynamics. *J. Molec. Graphics*, 14.1:33–38, 1996.

[46] Christoph R. Jacob, S. Maya Beyhan, and Lucas Visscher. Exact functional derivative of the nonadditive kinetic-energy bifunctional in the long-distance limit. *J. Chem. Phys.*, 126:234116, 2007.

[47] Christoph R. Jacob, Johannes Neugebauer, and Lucas Visscher. A Flexible Implementation of Frozen-Density Embedding for Use in Multilevel Simulations. *J. Comput. Chem.*, 29:1011–1018, 2008.

[48] Christoph R. Jacob and Lucas Visscher. Calculation of Nuclear Magnetic Resonance Shieldings Using Frozen-Density Embedding. *J. Chem. Phys.*, 125:194104, 2006.

[49] Benjamin Kaduk, Tim Kowalczyk, and Troy Van Voorhis. Constrained Density Functional Theory. *Chem. Rev.*, 112:321–370, 2012.

[50] Ruslan Kevorkyants, Xiqiao Wang, David M. Close, and Michele Pavanello. Calculating Hyperfine Couplings in Large Ionic Crystals Containing Hundreds of QM Atoms: Subsystem DFT is the Key. *J. Phys. Chem. B*, 117:13967–13974, 2013.

[51] Karin Kiewisch, Georg Eickerling, Markus Reiher, and Johannes Neugebauer. Topological analysis of electron densities from Kohn–Sham and subsystem density functional theory. *J. Chem. Phys.*, 128:044114, 2008.

[52] J. P. Klinman. The Copper-Enzyme Family of Dopamine -Monooxygenase and Peptidylglycine -Hydroxylating Monooxygenase: Resolving the Chemical Pathway for Substrate Hydroxylation. *J. Biol. Chem.*, 281:3013–3016, 2005.

[53] W. Kohn and L. J. Sham. Self-Consistent Equations Including Exchange and Correlation Effects. *Phys. Rev.*, 140:1133–1138, 1965.

[54] Tim Kowalczyk, Shane R. Yost, and Troy Van Voorhis. Assessment of the δscf density functional theory approach for electronic excitations in organic dyes. *J. Chem. Phys.*, 134(5):054128, 2011.

[55] Alisa Krishtal, Debalina Sinha, Alessandro Genova, and Michele Pavanello. Subsystem Density-Functional Theory as an Effective Tool for Modeling Ground and Excited States, their Dynamics, and Many-Body Interactions. *J. Phys.: Condens. Matter*, 27:183202, 2015.

[56] Tomas Kubar and Marcus Elstner. Efficient Algorithms for the Simulation of Non-Adiabatic Electron Transfer in Complex Molecular Systems: Application to DNA. *Phys. Chem. Chem. Phys.*, 15:5794–5813, 2013.

[57] Sven Larsson. Electron transfer in chemical and biological systems. Orbital rules for nonadiabatic transfer. *J. Am. Chem. Soc.*, 103:4034–4040, 1981.

[58] Benjamin G. Levine, Chaehyuk Ko, Jason Quenneville, and Todd J. MartÍnez. Conical intersections and double excitations in time-dependent density functional theory. *Mol. Phys.*, 104(5-7):1039–1051, 2006.

[59] Steffen Lindert, Denis Bucher, Peter Eastman, Vijay Pande, and J. Andrew McCammon. Accelerated Molecular Dynamics Simulations with the AMOEBA Polarizable Force Field on Graphics Processing Units. *J. Chem. Theory Comput.*, 9:4684–4691, 2013.

[60] F. London. On the Theory of Non-Adiabatic Reactions. *Z. Phys.*, 74:143, 1932.

[61] Per-Olov Löwdin. Studies in Perturbation Theory: Part I. An Elementary Iteration-Variation Procedure for Solving the Schrödinger Equation by Partitioning Technique. *J. Mol. Spectrosc.*, 10:12–33, 1963.

[62] Eduardo V. Ludeña and Valentin V. Karasiev. *KINETIC ENERGY FUNCTIONALS: HISTORY, CHALLENGES AND PROSPECTS*, chapter 22, pages 612–665. 2002.

[63] Neepa T. Maitra. Perspective: Fundamental aspects of time-dependent density functional theory. *J. Chem. Phys.*, 144:220901, 2016.

[64] Neepa T. Maitra, Fan Zhang, Robert J. Cave, and Kieron Burke. Double excitations within time-dependent density functional theory linear response. *J. Chem. Phys.*, 120:5932–5937, 2004.

[65] R. A. Marcus. On The Theory Of Oxidation-Reduction Reactions Involving Electron Transfer .1. *J. Chem. Phys.*, 24:966–978, 1956.

[66] R.A. Marcus. Superexchange versus an intermediate BChl- mechanism in reaction centers of photosynthetic bacteria. *Chem. Phys. Lett.*, 133:471–477, 1987.

[67] G. Martins, A. M. Ferreira-Rodrigues, F. N. Rodrigues, G. G. B. de Souza, N. J. Mason, S. Eden, D. Duflot, J.-P. Flament, S. V. Hoffmann, J. Delwiche, M.-J. Hubin-Franskin, and P. Limao-Vieira. Valence shell electronic spectroscopy of isoprene studied by theoretical calculations and by electron scattering, photoelectron, and absolute photoabsorption measurements. *Phys. Chem. Chem. Phys.*, 11:11219–11231, 2009.

[68] Reinhard J. Maurer and Karsten Reuter. Assessing computationally efficient isomerization dynamics: δscf density-functional theory study of azobenzene molecular switching. *J. Chem. Phys.*, 135(22):224303, 2011.

[69] Michael G. Mavros and Troy Van Voorhis. Communication: CDFT-CI couplings can be unreliable when there is fractional charge transfer. *J. Chem. Phys.*, 143:231102, 2015.

[70] I. Mayer. On Lowdin's method of symmetric orthogonalization. *Int. J. Quantum Chem.*, 90:63–65, 2002.

[71] R. McWeeny. *Methods of Molecular Quantum Mechanics.* Academic Press, San Diego, 1992.

[72] C. A. Mead and D. G. Truhlar. Conditions For The Definition Of A Strictly Diabatic Electronic Basis For Molecular-Systems. *J. Chem. Phys.*, 77:6090–6098, 1982.

[73] Benedetta Mennucci. Modeling environment effects on spectroscopies through QM/classical models. *Phys. Chem. Chem. Phys.*, 15:6583–6594, 2013.

[74] Agostino Migliore. Full-electron calculation of effective electronic couplings and excitation energies of charge transfer states: Application to hole transfer in DNA π-stacks. *J. Chem. Phys.*, 131:114113, 2009.

[75] Agostino Migliore. Non-orthogonality problem and effective electronic coupling calculation: Application to charge transfer in p-stacks relevant to biochemistry and molecular electronics. *J. Chem. Theory Comput.*, 7:1712–1725, 2011.

[76] Agostino Migliore, Stefano Corni, Daniele Versano, Michael L. Klein, and Rosa Di Felice. First principles effective electronic couplings for hole transfer in natural and size–expanded DNA. *J. Phys. Chem. B*, 113:9402–9415, 2009.

[77] Kenneth J. Miller. Additivity methods in molecular polarizability. *J. Am. Chem. Soc.*, 112:8533–8542, 1990.

[78] Vicent Molina and Manuela Merchán. Theoretical analysis of the electronic spectra of benzaldehyde. *J. Phys. Chem. A*, 105(15):3745–3751, 2001.

[79] Frank Neese. The orca program system. *WIREs: Comput. Mol. Sci.*, 2(1):73–78, 2012.

[80] Johannes Neugebauer. Chromophore-Specific Theoretical Spectroscopy: From Subsystem Density Functional Theory to Mode-Specific Vibrational Spectroscopy. *Phys. Rep.*, 489:1–87, 2010.

[81] Johannes Neugebauer, Carles Curutchet, Aurora Munioz-Losa, and Benedetta Mennucci. A Subsystem TDDFT Approach for Solvent Screening Effects on Excitation Energy Transfer Couplings. *J. Chem. Theory Comput.*, 6:1843–1851, 2010.

[82] Johannes Neugebauer, Manuel J. Louwerse, Evert Jan Baerends, and Tomasz A.

Wesolowski. The merits of the frozen-density embedding scheme to model solvatochromic shifts. *J. Chem. Phys.*, 122:094115, 2005.

[83] M. D. Newton. Quantum Chemical Probes Of Electron-Transfer Kinetics - The Nature Of Donor-Acceptor Interactions. *Chem. Rev.*, 91:767–792, 1991.

[84] Abraham Nitzan. *Chemical Dynamics in Condensed Phases.* Oxford University Press, Oxford, 2006.

[85] Harald Oberhofer and Jochen Blumberger. Electronic coupling matrix elements from charge constrained DFT calculations using a plane wave basis set. *J. Chem. Phys.*, 133:244105, 2010.

[86] Harald Oberhofer and Jochen Blumberger. Revisiting electronic couplings and incoherent hopping models for electron transport in crystalline c60 at ambient temperatures. *Phys. Chem. Chem. Phys.*, 14:13846–13852, 2012.

[87] Vikas S. Padalkar and Shu Seki. Excited-state intramolecular proton-transfer (esipt)-inspired solid state emitters. *Chem. Soc. Rev.*, 45:169–202, 2016.

[88] Robert G. Parr and Weitao Yang. *Density-Functional Theory of Atoms and Molecules.* Oxford University Press, Oxford, 1989.

[89] Michele Pavanello. On the Subsystem Formulation of Linear-Response Time-Dependent DFT. *J. Chem. Phys.*, 138:204118, 2013.

[90] Michele Pavanello and Johannes Neugebauer. Linking the Historical and Chemical Definitions of Diabatic States for Charge and Excitation Energy Transfer Reactions in Condensed Phase. *J. Chem. Phys.*, 135:134113, 2011.

[91] Michele Pavanello and Johannes Neugebauer. Modelling Charge Transfer Reactions with the Frozen Density Embedding Formalism. *J. Chem. Phys.*, 135:234103, 2011.

[92] Michele Pavanello, Troy Van Voorhis, Lucas Visscher, and Johannes Neuge-bauer. An Accurate and Linear-Scaling Method for Calculating Charge-Transfer Excitation Energies and Diabatic Couplings. *J. Chem. Phys.*, 138:054101, 2013.

[93] John P. Perdew, Kieron Burke, and Matthias Ernzerhof. Generalized Gradient Approximation Made Simple. *Phys. Rev. Lett.*, 77:3865–3868, 1996.

[94] Jay W. Ponder, Chuanjie Wu, Pengyu Ren, Vijay S. Pande, John D. Chodera, Michael J. Schnieders, Imran Haque, David L. Mobley, Daniel S. Lambrecht, Robert A. DiStasio, Martin Head-Gordon, Gary N. I. Clark, Margaret E. John-son, and Teresa Head-Gordon. Current status of the amoeba polarizable force field. *J. Phys. Chem. B*, 114(8):2549–2564, 2010.

[95] Davin M. Potts, Caroline M. Taylor, Rajat K. Chaudhuri, and Karl F. Freed. The improved virtual orbital-complete active space configuration interaction method, a "packageable" efficientab initiomany-body method for describing electronically excited states. *J. Chem. Phys.*, 114:2592–2600, 2001.

[96] Satyam Priyadarshy, Spiros S. Skourtis, Steven M. Risser, and David N. Be-ratan. Bridge-mediated electronic interactions: Differences between Hamilto-nian and Green function partitioning in a non–orthogonal basis. *J. Chem. Phys.*, 104:9473–9481, 1996.

[97] Pablo Ramos and Michele Pavanello. Quantifying Environmental Effects on the Decay of Hole Transfer Couplings in Biosystems. *J. Chem. Theory Comput.*, 10:2546–2556, 2014.

[98] Pablo Ramos and Michele Pavanello. Performance of Frozen Density Embedding for Modeling Hole Transfer Reactions. *J. Phys. Chem. B*, 119:7541–7557, 2015.

[99] Pablo Ramos and Michele Pavanello. Constrained Subsystem Density-Functional Theory. *Phys. Chem. Chem. Phys.*, 18:21172, 2016.

[100] Hermann Rau and Erik Lueddecke. On the rotation-inversion controversy on photoisomerization of azobenzenes. experimental proof of inversion. *J. Am. Chem. Soc.*, 104(6):1616–1620, 1982.

[101] Marko Schreiber, Mario R. Silva-Junior, Stephan P. A. Sauer, and Walter Thiel. Benchmarks for electronically excited states: Caspt2, cc2, ccsd, and cc3. *J. Chem. Phys.*, 128(13):134110, 2008.

[102] GaryB. Schuster and Uzi Landman. The Mechanism of Long-Distance Radical Cation Transport in Duplex DNA: Ion-Gated Hopping of Polaron-Like Distortions. In G.B. Schuster, editor, *Longe-Range Charge Transfer in DNA I*, volume 236 of *Topics in Current Chemistry*, pages 139–161. Springer Berlin Heidelberg, 2004.

[103] Issaka Seidu, Mykhaylo Krykunov, and Tom Ziegler. The formulation of a constricted variational density functional theory for double excitations. *Mol. Phys.*, 112(5-6):661–668, 2014.

[104] G. Senatore and K. R. Subbaswamy. Density Dependence of the Dielectric Constant of Rare-Gas Crystals. *Phys. Rev. B*, 34:5754–5757, 1986.

[105] K. Senthilkumar, F. C. Grozema, F. M. Bickelhaupt, and L. D. A. Siebbeles. Charge transport in columnar stacked triphenylenes: Effects of conformational fluctuations on charge transfer integrals and site energies. *J. Chem. Phys.*, 119(18):9809–9817, 2003.

[106] K Senthilkumar, FC Grozema, CF Guerra, FM Bickelhaupt, FD Lewis, YA Berlin, MA Ratner, and LDA Siebbeles. Absolute rates of hole transfer in DNA. *J. Am. Chem. Soc.*, 127:14894–14903, 2005.

[107] Sangwoo Shim, Patrick Rebentrost, Stéphanie Valleau, and Alán Aspuru-Guzik.

Atomistic study of the long-lived quantum coherences in the fenna-matthews-olson complex. *Biophys. J.*, 102(3):649 – 660, 2012.

[108] Mario R. Silva-Junior, Marko Schreiber, Stephan P. A. Sauer, and Walter Thiel. Benchmarks for electronically excited states: Time-dependent density functional theory and density functional theory based multireference configuration interaction. *J. Chem. Phys.*, 129(10):104103, 2008.

[109] Baljinder Singh, Monika Rani, Janpreet Singh, Lovika Moudgil, Prateek Sharma, Sanjeev Kumar, G. S. S. Saini, S. K. Tripathi, Gurinder Singh, and Aman Kaura. Identifying the preferred interaction mode of naringin with gold nanoparticles through experimental, dft and tddft techniques: insights into their sensing and biological applications. *RSC Adv.*, 6:79470–79484, 2016.

[110] Spiros S. Skourtis, David N. Beratan, and Jose Nelson Onuchic. The two-state reduction for electron and hole transfer in bridge-mediated electron-transfer reactions. *Chem. Phys.*, 176(2-3):501–520, 1993.

[111] Alisa Solovyeva, Michele Pavanello, and Johannes Neugebauer. Describing long-range charge-separation processes with subsystem density-functional theory. *J. Chem. Phys.*, 140:164103, 2014.

[112] G. te Velde, F. M. Bickelhaupt, E. J. Baerends, S. J. A. van Gisbergen, C. Fonseca Guerra, J. G. Snijders, and T. Ziegler. Chemistry with ADF. *J. Comput. Chem.*, 22:931–967, 2001.

[113] Alex J. W. Thom and Martin Head-Gordon. Hartree–Fock solutions as a quasidiabatic basis for nonorthogonal configuration interaction. *J. Chem. Phys.*, 131:124113, 2009.

[114] Troy Van Voorhis, Tim Kowalczyk, Benjamin Kaduk, Lee-Ping Wang, Chiao-

Lun Cheng, and Qin Wu. The Diabatic Picture of Electron Transfer, Reaction Barriers, and Molecular Dynamics. *Annu. Rev. Phys. Chem.*, 61:149–170, 2010.

[115] Prakash Verma, Wallace D. Derricotte, and Francesco A. Evangelista. Predicting near edge x-ray absorption spectra with the spin-free exact-two-component hamiltonian and orthogonality constrained density functional theory. *J. Chem. Theory Comput.*, 12(1):144–156, 2016.

[116] A. A. Voityuk, N. Rösch, J. Jortner, and M. Bixon. Superexchange Mediated Charge Hopping in DNA. *J. Phys. Chem. A*, 1:7599–7606, 2002.

[117] Alexander A. Voityuk. Electronic Couplings and On-Site Energies for Hole Transfer in DNA: Systematic Quantum Mechanical/Molecular Dynamic Study. *J. Chem. Phys.*, 128:115101, 2008.

[118] Alexander A. Voityuk. Electronic coupling for charge transfer in donor-bridge-acceptor systems. Performance of the two-state FCD model. *Phys. Chem. Chem. Phys.*, 14:13789–13793, 2012.

[119] Alexander A. Voityuk, Joshua Jortner, M. Bixon, and Notker Rösch. Electronic coupling between Watson-Crick pairs for hole transfer and transport in desoxyribonucleic acid. *J. Chem. Phys.*, 114:5614, 2001.

[120] Zhi Wang, Shu-Shen Li, and Lin-Wang Wang. Efficient real-time time-dependent density functional theory method and its application to a collision of an ion with a 2d material. *Phys. Rev. Lett.*, 114:063004, Feb 2015.

[121] T. A. Wesolowski. One-Electron Equations for Embedded Electron Density: Challenge for Theory and Practical Payoffs in Multi-Level Modeling of Complex Polyatomic Systems. In J. Leszczynski, editor, *Computational Chemistry: Reviews of Current Trends*, volume 10, pages 1–82. World Scientific, Singapore, 2006.

[122] T. A. Wesolowski, H. Chermette, and J. Weber. Accuracy of approximate kinetic energy functionals in the model of Kohn-Sham equations with constrained electron density: The FH$\cdots$NCH complex as a test case. *J. Chem. Phys.*, 105:9182, 1996.

[123] T. A. Wesolowski and A. Warshel. Frozen Density Functional Approach for *ab Initio* Calculations of Solvated Molecules. *J. Chem. Phys.*, 97:8050, 1993.

[124] T. A. Wesolowski and J. Weber. Kohn-Sham Equations with Constrained Electron Density: An Iterative Evaluation of the Ground-State Electron Density of Interacting Molecules. *Chem. Phys. Lett.*, 248:71–76, 1996.

[125] Tomasz A. Wesolowski. Embedding potentials for excited states of embedded species. *J. Chem. Phys.*, 140(18):18A530, 2014.

[126] Kenneth B. Wiberg, Christopher M. Hadad, James B. Foresman, and William A. Chupka. Electronically excited states of ethylene. *J. Phys. Chem.*, 96(26):10756–10768, 1992.

[127] Qin Wu, Benjamin Kaduk, and Troy Van Voorhis. Constrained density functional theory based configuration interaction improves the prediction of reaction barrier heights. *J. Chem. Phys.*, 130:034109, 2009.

[128] Qin Wu and Troy Van Voorhis. Direct optimization method to study constrained systems within density-functional theory. *Phys. Rev. A*, 72:024502, 2005.

[129] Qin Wu and Troy Van Voorhis. Extracting electron transfer coupling elements from constrained density functional theory. *J. Chem. Phys.*, 125:164105, 2006.

[130] Song Zhang, Simei Sun, Miaomiao Zhou, Lian Wang, and Bing Zhang. Ul-

trafast investigation of photoinduced charge transfer in aminoanthraquinone pharmaceutical product. *Scientific Reports*, 7:43419, 2017.

[131] Tom Ziegler, Mykhaylo Krykunov, and John Cullen. The implementation of a self-consistent constricted variational density functional theory for the description of excited states. *J. Chem. Phys.*, 136(12):124107, 2012.

[132] Tom Ziegler, Arvi Rauk, and Evert J. Baerends. On the calculation of multiplet energies by the hartree-fock-slater method. *Theor. Chem. Acc.*, 43(3):261–271, Sep 1977.

[133] Tom Ziegler, Michael Seth, Mykhaylo Krykunov, Jochen Autschbach, and Fan Wang. On the relation between time-dependent and variational density-functional theory approaches for the determination of excitation energies and transition moments. *J. Chem. Phys.*, 130:154102, 2009.

[134] George Zimmerman, Lue-Yung Chow, and Un-Jin Paik. The photochemical isomerization of azobenzene1. *J. Am. Chem. Soc.*, 80(14):3528–3531, 1958.

[135] Paul M. Zimmerman, Zhiyong Zhang, and Charles B. Musgrave. Singlet fission in pentacene through multi-exciton quantum states. *Nat. Chem.*, 2(8):648–652, 2010.